Facultad
de
Ciencias

RESPUESTA DE UN BIOSENSOR PLASMÓNICO METÁLICO NANOAGUJEREADO PARA LA MONITORIZACIÓN DE CÉLULAS BIOLÓGICAS

Optical Response of a Golden Plasmonic Device with Nanoholes to Asses Biological Cells

Trabajo de Fin de Grado
para acceder al

GRADO EN FÍSICA

Autor: Pablo Andrés Arnaiz
Directores: Francisco González Fernández
Fernando Moreno Gracia

Septiembre 2019

Contents

List of Figures

Acknowledgement

Firstly, I would like to thank Fernando and Paco for the warm welcome to their group, their generosity and all the help provided. Secondly, I would not have been able to complete this research without the support of a brilliant and widely wise person who has guided my work like a big sister. Thank you Ángela for your kindness, patience and attention.

Thanks to my family, because they know what I need exactly when I need it, because they have done their best for me to be here today. Particularly, thank you dad for your advice and supervision on cell Biology. Thank you Tom for brightening my life during this burdensome year and, of course, for checking my English grammar and vocabulary.

Special mention to Brown University, which has provided me with the time, place and motivation to write this dissertation. Thanks to my American troop of Spanish roommates, because they have seen this work grow at the same pace as its writer.

And last but definitely not least, thanks to each and every of my 11 classmates, my second family, with whom I have been honoured to share these intense five years at university.

To Ángela, Tom and my family

"Music is the arithmetic of sounds
as Optics the geometry of light"
Claude Debussy

Abstract

We have studied the optical response of a 60-nm-thick gold film with circular apertures of radius 90 nm, perforated periodically every 500 nm. Special attention was paid to the wavelength and transmittance changes at the extraordinary optical transmission peak for biological cells with different properties, which were immersed in a water solution on top of the sensor. The problem was computationally solved using two geometrical models in COMSOL. Particularly, we have studied the influence of the cell membrane and size, its cytoplasmic index, the contact length between cell and sensor, and some nuclear properties such as its refractive index, size and location. Finally, the overall behaviour of the device is reported for two samples of 50 lymphocytes and circulating tumour cells coming from a colorectal primary tumour. We have demonstrated that the sensor can discern these two cell types with an accuracy greater than 66%.

Key words: Plasmonics, Extraordinary Optical Transmission (EOT), Criculating Tumour Cell (CTC), Lymphocyte, Biosensor, COMSOL.

Resumen

Se ha estudiado la respuesta óptica de una placa de oro de 60 nm de anchura con aperturas circulares de radio 90 nm y perforadas con una periodicidad de 500 nm. Se ha observado el cambio de longitud de onda y transmitancia en el pico de transmisión óptica extraordinaria para células biológicas de diferentes características inmersas en una solución acuosa ubicada sobre el sensor. Mediante dos modelos geométicos bidimensionales se ha resuelto computacionalemente el problema en COMSOL. En particular, se ha observado la influencia de la membrana y el tamaño celulares, el índice citoplasmático, la longitud de contacto célula-placa y las propiedades del núcleo (índice de refracción, tamaño y posición). Finalmente, se ha comparado globalmente el comportamiento del sensor para dos muestras de 50 linfocitos y células tumorales circulantes procedentes de un cáncer colorrectal como tumor primario. Se ha demostrado una eficiencia del sensor en la discriminación linfocito-célula tumoral superior al 66%.

Palabras clave: Plasmónica, Transmisión Óptica Extraordinaria (EOT), Célula Tumoral Circulante (CTC), Linfocito, Biosensor, COMSOL.

Chapter 1

Introduction

1.1 Introductory Remarks on Plasmonics

Plasmonics forms a major field of research in the subject of nanophotonics, which explores the confinement of electromagnetic fields over dimensions on the order of or smaller than the wavelength. It is based on the interaction between electromagnetic waves and conduction electrons at metallic interfaces or in small metallic nanostructures. There exist mainly two objects of study in this field, namely surface plasmon polaritons and localised surface plasmons, which were firstly described at the very beginning of the XX century. These take the form of freely propagating electron density waves along metal surfaces and localised charge oscillations in metal nanoparticles.

In the visible range, the first observation of propagating surface plasmons on metal films dates from 1902, when Robert Wood announced some anomalous intensity patterns in spectra produced when light reflected at metallic gratings. These could not be explained by Kirchhoff's theory of diffraction and were later known as Wood anomalies. The origin of these anomalies was physically described in 1941 by Ugo Fano, who suggested the excitation of surface waves. Later in 1968, detailed experiments conducted by Raether and Kretschman, and the theoretical work of Ritchie connected these excitations with surface plasmons. As a result, a unified description of all these phenomena in the form of surface plasmon polaritons was established. During the following decades, a variety of new applications for metallic nanostructures was discovered, as well as an important milestone in Plasmonics, the extraordinary optical transmission [21]. In 1998, Thomas Ebbesen and his coworkers reported on the unusually high transmission of light through subwavelength metal nanoholed structures, apparently contradicting Bethe's diffraction theory (1994) for small apertures. With regards to the History of localised surface plasmons, even the Romans unintentionally used localised plasmonic resonances in gold and silver colloidal nanoparticles to impress their contemporaries with cups that changed their colour depending on the position they were lit from. It was not until 1908, when Mie developed a solid mathematical foundation explaining such phenomena.

Quoting Bill Barnes from the University of Exeter, my host institution during my year abroad: "In Plasmonics you just have Maxwell's equations, some material properties and

boundary conditions, all classical stuff; what's new about that? No new fundamental particles, no new cosmology, but surprises, adventure and a wide range of applications - solar cells, high-resolution microscopy, drug design and many more. Plasmonics is one of those small-scale topics where good people can do interesting things with modest resources."

1.2 Motivation

During my third year as an undergraduate in Physics, professors Moreno and González introduced a lecture on a promising and interdisciplinary project they had just undertaken. It was about the use of a nanostructured golden film to improve cancer diagnosis and its treatment. A few months later, during my Erasmus exchange in Exeter, I was enrolled in a course about the Physics of nanostructures, particularly their optical properties which included the concept of plasmon. Amazed by the potential applications of Plasmonics, I could not reject the incredible offer to investigate this topic as part of my final undergraduate dissertation.

By the time I took part in this project, vast experimental research had already been done on the applications of a golden nanostructured array of holes to distinguish between cancerous and healthy human cells. On the contrary, the theoretical explanation of our device's optical response was not as advanced as the thriving experimental results. Barreda and her coworkers [6] conducted preliminary simulations to study the effects on the positions (wavelengths) of the transmission maxima when certain objects with various shapes were located on top of the film. At the end of this study they focused more specifically on a simplistic model of the cell, considered as a homogeneous sphere with a constant refractive index. Using this model, they only reported on the dependence of the wavelengths at maxima under variations of the refractive index and cell deformation.

My task in this project consists of deepening into the computational approach by giving a more detailed description of the influence that each part of the cell has upon the overall behaviour. Ideally, these simulations conducted for realistic samples of cells, should reproduce the already obtained experimental results.

With this work I finalise my degree in Physics having actively used a great deal of concepts learnt throughout my academic studies. Particularly, optical theories, such as diffraction and interference were employed, as well as Drude's model to describe metals, covered in modules about Solid State Physics.

1.3 Main Purposes and Work Structure

As already mentioned, this work seeks to deepen into the theoretical understanding of a gold film with nanoholes when cells are located on top of it and they are immersed in a water solution. Particularly, we want to focus on the optical response dependent on the properties of the cell. The two primary goals are:

- Study the cell using a more detailed computational model, including its membrane,

cytoplasm and nucleus. Attention will not only be paid to the wavelengths at transmission maxima, but also their transmittances.

- Simulate two realistic samples of lymphocytes and tumour cells in order to obtain a combined description of the behaviour under both cell types.

In particular, there are seven cellular properties we aim to evaluate: cell size, cytoplasmic refractive index, presence of a membrane, degree of contact with the film, nuclear size, nuclear refractive index and nuclear positioning. For each of these, a particular maximum in the transmission spectra is studied, whose transmittance and wavelength (only in some cases) are reported for a range of values. Finally, we pursue a representation of the transmittance change against wavelength shifting with respect to the free film for the two samples of fifty lymphocytes and cancerous cells. The goal is to explain where cells are located in this map, according to the individual properties studied prior to the combined approach.

The second chapter is dedicated to a detailed description of the Physics behind the metal nanostructure, including the excitation of surface plasmon polaritons as well as the phenomenon of extraordinary optical transmission. Chapter three shows the necessary information about molecular Biology of the cell to understand its optical and structural properties. In the fourth chapter a detailed explanation of the device is reviewed as well as the computational methods to simulate its behaviour. The last two chapters aim to provide the reader with an ordered presentation of the results, some conclusions and possible future directions to continue this research.

Chapter 2

Theory and Optical Properties of Plasmonic Devices with Nanoholes

This chapter reviews the concepts of plasmon and extraordinary optical transmission to acquire the physical background involved in the optical response of a metallic nanoholed plate to be used as a biosensor.

2.1 Dielectric Function of the Electron Gas

The interaction of metals with light can be accurately understood from a classical point of view based on Maxwell's equations. Even metallic nanostructures down to sizes of the order of a few nanometers can be described without a need to use Quantum Mechanics, since the high density of free carriers results in very small spacings of the electron energy levels compared to thermal excitations of energy k_BT at room temperature [21].

Over a wide frequency range, the optical properties of metals can be explained by **Drude's model**, where a gas of free electrons of density n moves against a background of positive ion cores. Neither electron-electron interactions nor details of the lattice potential will be taken into account, as it can be assumed that their effects are incorporated into the effective mass m of each electron. Electrons oscillate in response to the applied electromagnetic field, and their motion is damped by the collisions occurring with a characteristic collision frequency $\gamma = 1/\tau$, where τ is the relaxation time of the free electron gas, which is typically in the order of 10^{-14} s at room temperature, corresponding to $\gamma \sim 100$ THz. One can write a simple equation of motion for an electron of the gas under an external electric field $\vec{E}(t) = \vec{E_0}e^{-i(\omega t + \vec{k}\vec{r} + \varphi_0)}$, corresponding to a plane wave [17, 21]:

$$m\frac{d^2\vec{x}}{dt^2} + m\gamma\frac{d\vec{x}}{dt} = -e\vec{E} \quad \Longrightarrow \quad \vec{x}(t) = \frac{e}{m(\omega^2 + i\gamma\omega)}\vec{E}(t). \tag{2.1}$$

The dipole moment of one electron is $e\vec{x}$ and the polarisation $\vec{P}$, defined as the dipole moment per unit of volume and verifying $\vec{D} = \varepsilon_0\vec{E} + \vec{P}$, is

$$\vec{P} = -\frac{ne^2}{m(\omega^2 + i\gamma\omega)}\vec{E}(t) \quad \Longrightarrow \quad \vec{D} = \varepsilon_0\left(1 - \frac{\omega_p^2}{\omega^2 + i\gamma\omega}\right)\vec{E}(t), \tag{2.2}$$

where $\vec{D}$ is the electric displacement field and $\omega_p^2 = \frac{ne^2}{\varepsilon_0 m}$ the **plasma frequency**, which corresponds to the natural frequency of a free oscillation of the electron sea. Therefore, the dielectric function is

$$\varepsilon(\omega) = 1 - \frac{\omega_p^2}{\omega^2 + i\gamma\omega} \approx 1 - \frac{\omega_p^2}{\omega^2}, \tag{2.3}$$

where the last approximation holds for large frequencies, such as the visible regime. In a nonmagnetic isotropic medium the electromagnetic wave equation is expressed as [17]

$$\mu_0 \frac{\partial^2 \vec{D}}{\partial t^2} = \nabla^2 \vec{E} \quad \Longrightarrow \quad \varepsilon(\omega)\varepsilon_0\mu_0\omega^2 = k^2. \tag{2.4}$$

As a result, if ε is positive ($\omega > \omega_P$), the electromagnetic wave propagates transversely through the material with a refractive index $n = \sqrt{\varepsilon}$ and electrons do not oscillate in phase with the field, as occurs in dielectrics. In this case, the electron gas is said to be transparent. If ϵ is negative ($\omega < \omega_P$), then the electromagnetic wave is damped by the metal and the refractive index is complex. Free electrons follow the external disturbance and oscillate at the same frequency as the electric field until the perturbation is attenuated after a few nanometers. Incident waves on the medium in this frequency region do not propagate, but will be totally reflected [17].

2.2 Surface Plasmons

Surface plasmons are free electron oscillations existing at the interface between two materials with opposite signs in the real part of their dielectric functions, such as a metal (negative) and a dielectric (positive). They propagate in the longitudinal direction to the interface and are evanescently confined in the perpendicular direction. A surface plasmon confined in a nanoparticle of size comparable to or smaller than the wavelength of light used to excite the plasmon is called **localized surface plasmon**. The coupling of the charge motion in the metal (surface plasmon) to the electromagnetic field in the dielectric (polariton) is called **surface plasmon polariton** (SPP) [21], as shown in figure 2.1.

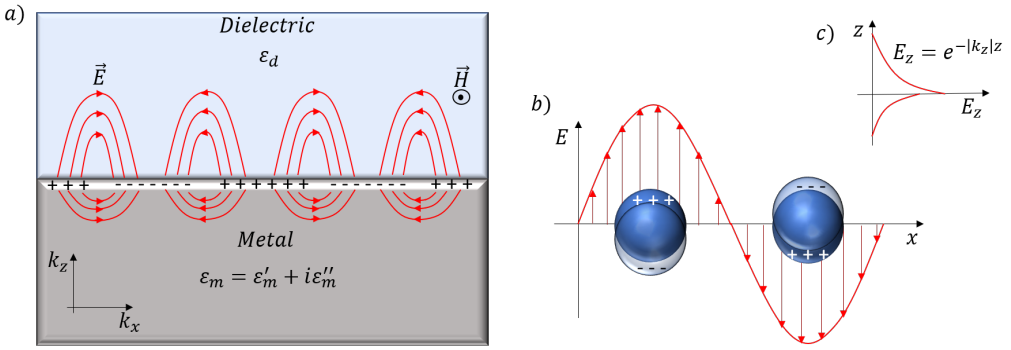

Figure 2.1: a) SPP propagating on a dielectric-metal interface in the x direction. H_y represents the magnetic field in the y direction. b) Localised surface plasmon. c) Exponential dependence of the field E_z.

By combining equations 2.3 and 2.4 in the transparency regime, the following dispersion relation for surface plasmons holds

$$\omega^2 = \omega_p^2 + c^2 k^2. \tag{2.5}$$

For good metals, such as Au, Ag or Cu, with dielectric constant $\varepsilon_m = \varepsilon'_m + i\varepsilon''_m$ and verifying $\varepsilon''_m << |\varepsilon'_m|$, the dispersion relation of a SPP, characterised by the wave-vector $\vec{k}_{SPP}$, can be expressed as [26, 27]

$$k_{SPP} = \frac{\omega}{c}\left(\frac{\varepsilon_d \varepsilon'_m}{\varepsilon_d + \varepsilon'_m}\right)^{1/2} \quad \Longrightarrow \quad \lambda_{SPP} = \lambda\left(\frac{\varepsilon_d + \varepsilon'_m}{\varepsilon_d \varepsilon'_m}\right)^{1/2}, \tag{2.6}$$

where $\lambda_{SPP} = 2\pi\frac{c}{\omega}$ is the wavelength in vacuum and ε_d the dielectric's dielectric constant. For good metals and negligible damping constant, the asymptotic behaviour of the frequency, reached at large wave-number values, is

$$\omega_{SPP} = \frac{\omega_p}{(1+\varepsilon_d)^{1/2}}. \tag{2.7}$$

Figure 2.2 shows the dispersion relation of surface plasmons and SPPs according to the precedent equations as well as the linear dispersion of light within the dielectric.

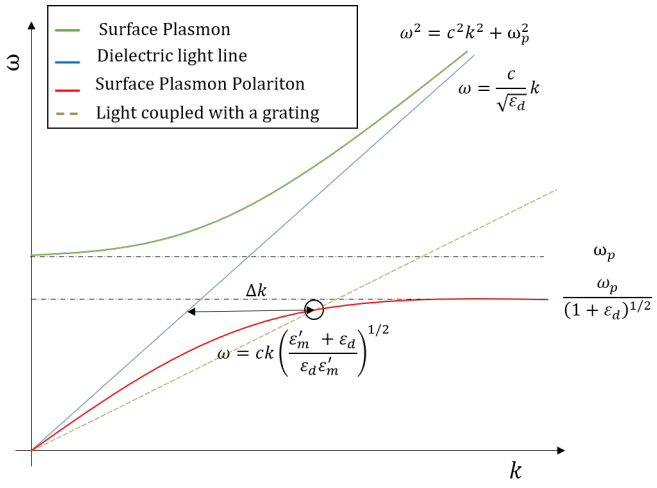

Figure 2.2: Dispersion relation of surface plasmons, SPPs and light, both within the dielectric and coupled to a grating.

An important property of SPPs is their field penetration into the dielectric, δ_d, and the metal, δ_m. The latter is called **skin depth**. For good metals, these two quantities can be written as [27]

$$\begin{cases} \delta_d \approx \frac{\lambda\sqrt{|\varepsilon'_m|}}{2\pi\varepsilon_d} \\ \delta_m \approx \frac{\lambda}{2\pi\sqrt{|\varepsilon'_m|}}. \end{cases} \tag{2.8}$$

The penetration depth of the field into the dielectric provides us with a measure of the

length scale over which the SPP is sensitive to changes in the refractive index, for example the presence of certain bio-molecules in a biosensor. The skin depth measures the minimum required metal thickness for the sensor. In the case of an incident wavelength of $\lambda = 700$ nm, the metal being gold ($\varepsilon'_m = -16.5$ [16]) and water as dielectric ($\varepsilon_d = 1.77$), the SPP penetration into the latter would be $\delta_d \sim 250$ nm and the skin depth $\delta_m \sim 27$ nm.

As shown in figure 2.2, the SPP dispersion curve is below the light line, thus for a given frequency lower than ω_{SPP}, the SPP wave-number is always greater than that of the photon. In order to verify the momentum conservation law, so that a SPP can be optically excited, extra conditions are required. In other words, light in the visible and near-infrared range does not couple to surface plasmons on a smooth metal-dielectric interface and no SPP can be excited, since momentum conservation would be violated. However, periodic structures can provide the extra momentum needed to excite SPPs.

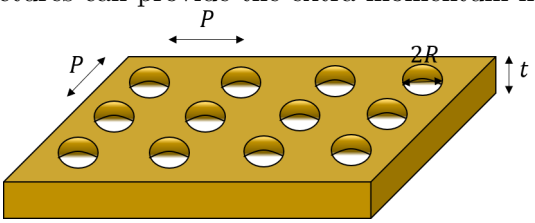

Figure 2.3: Golden grating of thickness t with holes of radius R periodically distributed in the x and y directions with period P.

Let us consider a metal grating with holes perforated periodically with period P, as shown in figure 2.3. Configurations like this give light the extra momentum needed to excite SPPs. Let $\vec{G}_x$ and $\vec{G}_y$ be the vectors of the reciprocal lattice in the x and y directions, where $|\vec{G}_x| = |\vec{G}_y| = 2\pi/P$. The interaction between the incident light and the surface plasmon is fulfilled when the following equation holds [13]

$$\vec{k}_{SPP} = \vec{k}_x \pm i\vec{G}_x \pm j\vec{G}_y, \tag{2.9}$$

where $\vec{k}_x$ is the x component of the incident wave-vector and i, j integers corresponding to the coordinates in the reciprocal lattice. This phenomenon can also be explained as a decrease in the slope of the dispersion relation of the incident wave (see figure 2.2). As a result, the light line and the SPP curve intersect at the value of k where the SPP is excited. For a given frequency, the increase of momentum Δk experienced by the light due to the grating is what makes the excitation of the SPP possible.

The condition in equation 2.9 and the dispersion relation in 2.6 impose certain vibration modes known as **surface plasmon-Bloch waves**. At normal incidence, these are given approximately by the wavelengths

$$\lambda_{SPP} = \frac{P}{(i+j)^{1/2}} \left(\frac{\varepsilon_d \varepsilon'_m}{\varepsilon_d + \varepsilon'_m} \right)^{1/2}. \tag{2.10}$$

Not only does the grating configuration provide incident light with the necessary extra momentum to excite SPPs, but in the case of nanometric holes it also shows interesting transmission effects that can only be explained through diffraction theory.

2.3 Diffraction and Extraordinary Optical Transmission

Diffraction is a physical phenomenon exclusively appearing when waves (light in our case) pass through an aperture or an obstacle. It is mainly perceptible when the object size is comparable to the wavelength. For long distances, diffraction can be understood by Fraunhoffer equation, a simplified version of the more general Kirchhoff's diffraction formula. The intensity of the Fraunhoffer diffraction pattern for a circular aperture of radius R at any point of a plane at distance f, corresponding to the focal distance of a convergent lens, is given by the squared modulus of the Fourier transform of the aperture [9]

$$I \propto \left(\frac{\lambda}{2\pi R} \frac{f}{\rho} J_1 \left(\frac{2\pi R}{\lambda} \frac{\rho}{f} \right) \right)^2, \tag{2.11}$$

where J_1 is the Bessel function of first order and ρ the radial coordinate in the focal plane. This pattern, showing an intense central maximum that concentrates over the 80% of the total intensity, is commonly known as Airy disc and is represented in figure 2.4.

Figure 2.4: Fraunhoffer diffraction pattern of a circular aperture known a Airy disc.

However, when a periodic holed array like in section 2.2 is considered, incident light is diffracted by a large number of circular apertures. The condition for constructive interference is given by Bragg's law

$$P \sin\theta = m\lambda, \tag{2.12}$$

where m is an integer referring to the diffraction order and θ the incidence angle. As can be inferred from equation 2.12, no diffraction order can be found for wavelengths greater than the period. Furthermore, equation 2.9 can be rewritten in such a way ($k_x = \frac{2\pi}{\lambda}\sqrt{\epsilon_d}\sin\theta$) that diffracted light by the grating can only couple to a surface plasmon if its momentum satisfies the following diffraction grating condition [15, 21]

$$\frac{2\pi}{\lambda} n_d \sin\theta + m\frac{2\pi}{P} = k_{SPP}, \tag{2.13}$$

where $n_d = \sqrt{\varepsilon_d}$. As stated previously, the grating condition is essential for the SPP excitation and this can be checked using the above equation when $P \longrightarrow \infty$. This limit, equivalent to no grating configuration, yields to an equality between the wave-number of light within the dielectric and that of the SPP, which is impossible as shown in figure 2.2.

In 1944 Hans Bethe found differences in the behaviour of diffraction with respect to Kirchhoff's theory when very small holes were considered. Particularly, he discovered that the normalised-to-area transmission through a subwavelength circular aperture perforated in an infinitely thin perfect conductor plate was

$$T = \frac{64}{27\pi^2}\left(\frac{R}{\lambda}\right)^4, \tag{2.14}$$

in contrast to the dependence on the second power predicted by Kirchhoff [5]. As a consequence, transmission decreases significantly with the hole radius, implying that a subwavelength hole in a thin metal plate is seemingly a poor device for transmitting light through.

However, in 1998 Ebbesen et al. [11] studied the optical properties of submicrometer cylindrical cavities in metallic films and found that arrays of such holes displayed highly unusual zero-order transmission spectra (where the incident and detected light are collinear) at wavelengths greater than the array period, beyond which no diffraction was presumed to occur. More significantly, sharp peaks in transmission were observed at wavelengths as large as twenty times the radius of the cylinders, whose maxima showed transmissions over the unity when normalised to the hole area, which is orders of magnitude greater than predicted by Bethe's theory. This phenomenon taking place in two-dimensional periodic arrays of subwavelength holes was therefore named as **extraordinay optical transmission** (EOT) and is inextricably linked to the presence of SPPs. We will henceforth distinguish between enhance transmission, when the array transmits more light per hole area than a single aperture, and EOT, if such normalised transmission is greater than one.

There exists another reason which may cause sharp maxima showing normalised-to-area transmissions greater than one, known as **Rayleigh anomaly**. Although firstly observed by Wood in 1902 when he was studying light spectra through metal gratings, Rayleigh justified the existence of such peaks as a change in the diffraction order to values different from zero, in other words, the scattered wave becomes tangential to the grating surface [12]. An approximate equation for the incident wavelength that excites these resonant maxima is [22]

$$\lambda_{RA} = \frac{n_d P}{(r+s)^{1/2}}, \tag{2.15}$$

where r and s are integers corresponding to the orders of this Rayleigh anomaly. It is worth emphasising that both EOT and Rayleigh anomalies show surprising peaks with unusually high transmissions, although their origin is different. EOT takes place when incident and detected beams are collinear or equivalently, when the diffraction order is zero, and it is related to the excitation of a SPP, whereas Rayleigh anomaly is due to a change in the diffraction order.

Figure 2.5 displays the transmission spectrum of the two-dimensional plasmonic device used in the present study, which will be thoroughly described in chapter 4. The three maxima exhibit a transmission normalised to the area occupied by holes of $T_1 = 0.61$, $T_2 = 2.17$ and $T_3 = 1.33$. In other words, maxima at $\lambda_2 = 635$ nm and $\lambda_3 = 769$ nm

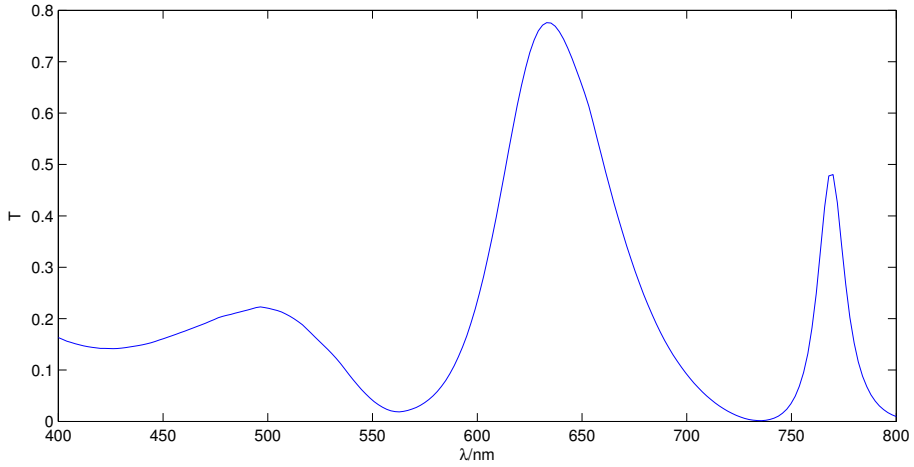

Figure 2.5: Transmission spectra corresponding to the 2D geometry of a periodically nanostructured gold film of thickness $t = 60$ nm, hole width $W = 180$ nm and period $P = 500$ nm sandwiched between two dielectric media made of water and glass.

show situations where more light is transmitted than the light hitting directly on the holes, which could be cases of EOT or Rayleigh anomaly. Furthermore, a single aperture would show normalised-to-area transmissions of the order of 10^{-3} in the visible range, which is insignificant compared to transmissions at the maxima. It is also worth noting in the above figure that the last two peaks appear at wavelengths greater than the period ($P = 500$ nm), expounding an anomalous behaviour when compared to Bethe's diffraction theory. In addition, the intensity of the zero-order transmission from a grating is expected to decrease monotonically at larger wavelengths [11]. Therefore, it can be inferred from this spectrum that the array itself is an active element, not just a passive geometrical object in the path of the incident beam.

In the configuration providing the above spectrum there exist two interfaces metal-dielectric, namely Au-Water and Au-glass. Consequently, it is possible to distinguish two different modes as a result of the interference between the SPPs at both interfaces. They are known as symmetric and antisymmetric and differ in their propagation distance, long for the symmetric and short for the antisymmetric [19]. When the film thickness is smaller than 2–3 skin-depths, these two modes interact and substantially couple one to another. In this case, the dispersion relations of film modes can differ from that of the SPP [27].

Although the two main peaks in figure 2.5 show normalised transmissions greater than one, they have different origins. The one at $\lambda_2 = 635$ nm cannot be explained by EOT. According to equation 2.15 and taking the Au-water interface into account ($n_d = 1.33$), the first order Rayleigh peak for $P = 500$ nm should appear at wavelength $\lambda_{RA} \approx 660$ nm, which corresponds to the peak labelled as λ_2. The last maximum at $\lambda_1 = 769$ nm can be identified with the SPP excitation, whose approximate theoretical value according to equation 2.10 is $\lambda_{SPP} \approx 700$ nm, therefore a case of EOT. Such important difference between simulated and theoretical values can be explained by the interaction between the

symmetric and antisymmetric modes in the gold plate, due to the film thickness $t = 60$ nm and its skin-depth $\delta_m = 27$ nm.

It has been studied [11, 27] that good metals like Au and Ag are significantly better for EOT than others such as Ni or Cr. The first ones allow the presence of much prominent and narrow maxima due to their lower absorption. On the other hand, other metals are characterised by a more diffuse spectrum with broader and less significant peaks. Periodicity is a key factor in the position of the peaks, which turns out to be proportional to the period of the lattice. In particular, theoretical calculations for perfect conductors ($\epsilon_m = \infty$) demonstrated a linear increase in the maxima location with respect to the period. Positions of peaks are also dependent upon the hole shape and size. In particular, there is plenty of research about the sensing application of gratings with rectangular and elliptical holes [26]. Regarding their size, it has been proven [27] that positions of maxima increase linearly with the hole radius. The thickness of the plate is also important, as the optimal conditions to excite SPPs, EOT and the coupling between the symmetrical and antisymmetrical modes are fulfilled when such thickness is between one and three skin depths. Furthermore, the width of the maxima appears to be strongly dependent on the ratio t/R [11], the smaller this value the broader the peaks.

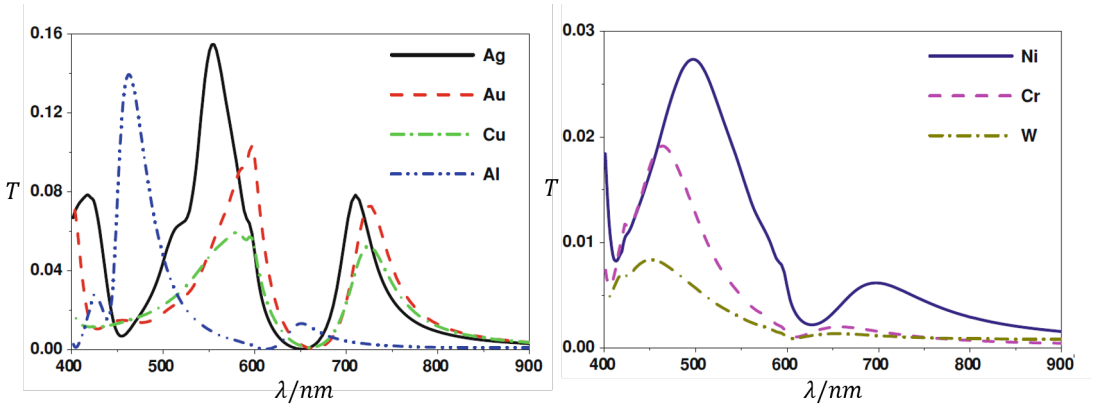

Figure 2.6: Transmission spectra for different metals when a three dimensional grating with circular holes and sandwiched between air and a dielectric ($\varepsilon_d = 2.25$) is considered. The geometrical parameters are: $P = 400$ nm, $t = 250$ nm and $R = 114$ nm.

Several spectra corresponding to three dimensional gratings for different metals are shown in figure 2.6. It can be inferred from them, that the EOT peak is only present in good metals (Au, Ag, Cu), where SPP excitations take place. Furthermore, shape and position of such maximum are not as dependent on the material and geometry as they are for the Rayleigh anomaly maximum, when compared to the spectrum showed in figure 2.5. More interestingly, the EOT peak position does not seem to be hugely dependent on dimension, since figure 2.6 shows a similar SPP resonant wavelength to the two dimensional simulations in figure 2.5, even for a lower period. On the contrary, transmission decreases significantly for realistic three dimensional configurations, in contrast to their two dimensional versions. Regarding the Rayleigh peak, appearing even for non-good metals, both its position and transmission strongly depend on the dimension, material and geometry.

Chapter 3

An Introduction to Cell Biology

The aim of this chapter is to give a general overview of the cell structure in order to describe the fundamentals of circulating tumour cells (CTC) in comparison to lymphocytes. Particularly, special attention will be paid to the optical properties of these two structures so that we can obtain a better understanding of the plasmonic device behaviour under the influence of such cellular types.

3.1 General Cytology

Eukaryotes, such as animals, are organisms made up of eukaryotic cells, that is to say, cells that contain a nucleus and organelles, which are immersed in the cytoplasm and enclosed by the plasma membrane. Each organelle has a specific function within the cell and their positions are established by the cytoskeleton, which is also involved in the cell mobility.

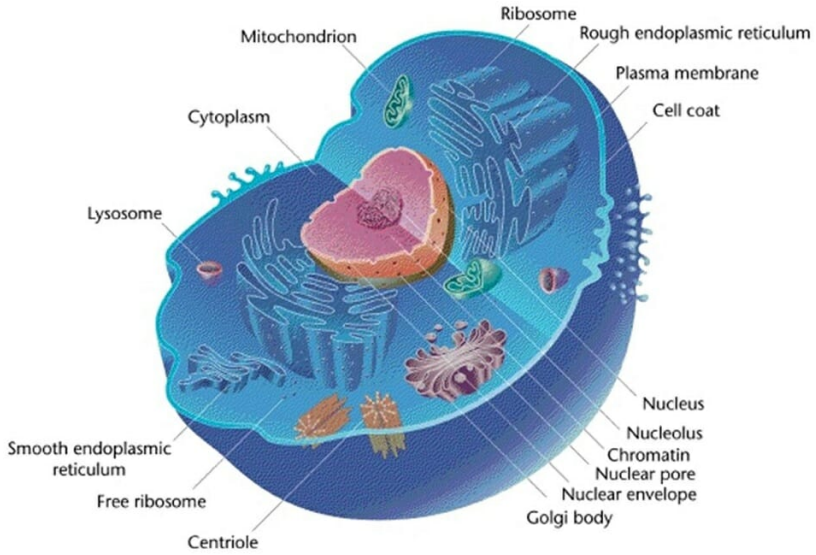

Figure 3.1: Scheme of an animal cell showing its main organelles.

The sizes of eukariotic cells depend very much on their type and may vary between 10 and 100 microns. They are mostly composed of water (above 70%) although non negligible

percentages of their mass are formed by proteins, lipids, nucleic acids, polysaccharides and inorganic ions. Cellular division takes place through two processes known as mitosis and meiosis, whose main difference is the level of similarity between the mother cell and its daughters. Mitosis gives rise to two genetically identical cells with replicated DNA, whereas a cell undergoing meiosis divides into four genetically distinct daughters. Among all the organelles, it is worth mentioning the self-replicating mitochondria for their use of oxygen to release energy stored in cellular nutrients (typically glucose) [3]. This process is conducted by generating adenosine triphosphate (ATP), a complex organic chemical that provides energy to drive many processes in living cells, known as the *molecular unit of currency of intracellular energy transfer*.

3.1.1 Plasma Membrane

This container acts as a selective barrier that enables the cell to concentrate nutrients gathered from its environment, retain the products it synthesizes and excrete the waste. The plasma membrane is formed by a thin phospholipid bilayer (5-10 nm) combined with several types of proteins. Such phospholipids have the property of being amphiphilic, that is to say, they can either behave as hydrophobic molecules (water-insoluble) or hydrophilic (water-soluble). Due to its selective permeability, the membrane facilitates the movement of specific molecules in and out of cells. Membrane proteins also account for specific and selective interactions with their extracellular environment, including the adhesion of cells to other cells, their attachment to surfaces and communication between them [3].

3.1.2 Cytoplasm

Every component of the cell enclosed by the plasma membrane except for the nucleus is known as cytoplasm. It includes a water-based solution known as cytosol where organalles, proteins and other substances such as glycogen and lipids float. Approximately, an 80% of the cytoplasmic mass corresponds to water. The cytosol, having a pH that lies very slightly on the alkaline side of neutrality, at about 7.2, mainly contains dissolved proteins, amino acids, sugars and ions. Its viscosity is roughly the same as pure water, although diffusion of small molecules from a region of higher concentration to a region of lower concentration through this liquid is about fourfold slower than in pure water. This phenomenon takes place due to collisions with the large number of organic macromolecules such as proteins, whose concentration could reach 20-30% in volume. In contrast to extracellular fluids, cytosol has a high concentration of potassium ions and a low concentration of sodium ions. This difference in ion concentrations is critical for osmoregulation, since if the ion levels were the same inside a cell as out of it, water would enter constantly by osmosis [8].

For cells to function properly, they must organise themselves in space and interact mechanically with their environment. They have to be correctly shaped, physically robust and properly structured internally. Furthermore, they must rearrange their internal components as they grow and divide, and even change their shape to move around. All these tasks are performed by a set of tubules and filaments placed in the cytoplasm, known as **cytoskeleton**. The three main components of this cytoskeleton are actin filaments, which

determine the shape of the cell's surface and are necessary for the cell motion, intermediate keratin filaments, that provide mechanical strength, and microtubules, determining the position of the organelles and leading intracellular transport [3].

3.1.3 Nucleus

The nucleus is a highly specialised organelle that serves as the information processing centre of the cell. This organelle has two major functions: it stores the cell's genetic material (DNA) and it coordinates the cell's activities, such as growth, intermediary metabolism, protein synthesis, and cell division. Its size compared to that of the whole cell can vary very much from one cell to another; on average the nucleus occupies the 10% of the cell's volume, although there exist extreme cases, like lymphocytes, whose nuclei represent between the 70 and 90% of the whole volume [3, 8].

A double-layered membrane, known as nuclear envelope, separates the content of the nucleus from the cytoplasm. The envelope is perforated by holes called nuclear pores that allow specific types of molecules to pass back and forth between the nucleus and the cytoplasm. Most of the nucleus is occupied by the nucleoplasm, a semifluid mainly composed of chromatin, which is a dense complex of DNA and protein whose primary function consists of packaging very long DNA molecules into a more compact DNA and is involved in the cell division. The nucleolus, floating in the nucleoplasm, synthesises protein-producing macromolecular assemblies called ribosomes.

3.2 Circulating Tumour Cells

During mitosis and meiosis some errors which may cause mutations are relatively likely to occur. In a human body, having more than 10^{14} cells, millions of cells experience mutations every day, potentially disrupting the social cellular order [3]. Most dangerously, a mutation may give one cell a selective advantage, allowing it to grow and divide faster, and survive more effectively than its neighbours. This situation is known as **tumour**. A tumour is considered a **cancer** if its cells have acquired the ability to invade surrounding tissue. This invasive tendency allows them to freely enter into the bloodstream and form secondary tumours. It is called **metastases** if several tissues have been affected. When a cancer has metastasised, the original organ where the initial abnormal cell started growing is called primary tumour.

Most commonly, cancer remains asymptomatic at the early stages and cannot be detected until late stages of its development. Due to the fact that patients showing metastases normally have low chances of survival, current research is focused on its origin and anticipated treatment [25]. Initially, the epithelial cells of a primary tumour approach nearby blood or lymphatic vessels and produce a protein called matrix metalloproteinase (MMP) which breaks the collagen fibres of the vessels and opens a free path for them to shed into the bloodstream, as figure 3.2 shows. During this process, epithelial cells must undergo epithelial to mesenchymal transition (EMT), which consists of a change in phenotype from a more specialised cell (epithelial) to a multipotent cell (mesenchymal) that

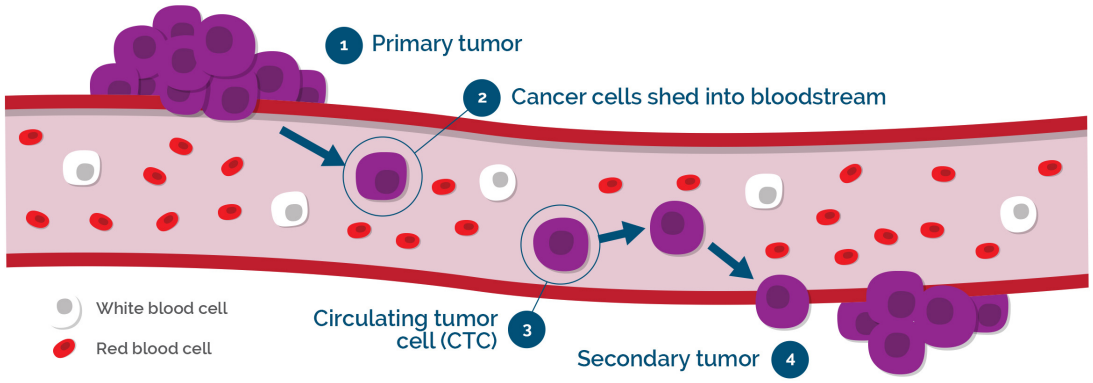

Figure 3.2: Scheme showing the process in which a tumour cell detaches from the primary tumour, sheds into the bloodstream and causes a secondary tumour.

can transform into a variety of cell types, as shown in figure 3.3. Such epithelial cell can detach itself from the parent tissue and become a free flowing entity called **circulating tumour cell** (CTC). Once into the bloodstream, they can approach other tissues and invade them. An aggressive tumour cell can attach itself to the endothelial membrane of the vessel and create a pore through which it leaves the circulatory system and invades the nearby tissue. Other less aggressive tumour cells may use this pore to enter the same tissue. These undifferentiated cells in the bloodstream can revert their phenotype by undergoing mesenchymal to epithelial transition (MET) out of which some can contribute to metastasis leading to cancer progression. After having changed their phenotype by MET, tumour cells can adhere to the wall of capillaries and then evade from them to nearby tissues. Since they can now behave as epithelial cells again, they attach themselves to the target site and start dividing, giving rise to a new tumour [25, 29].

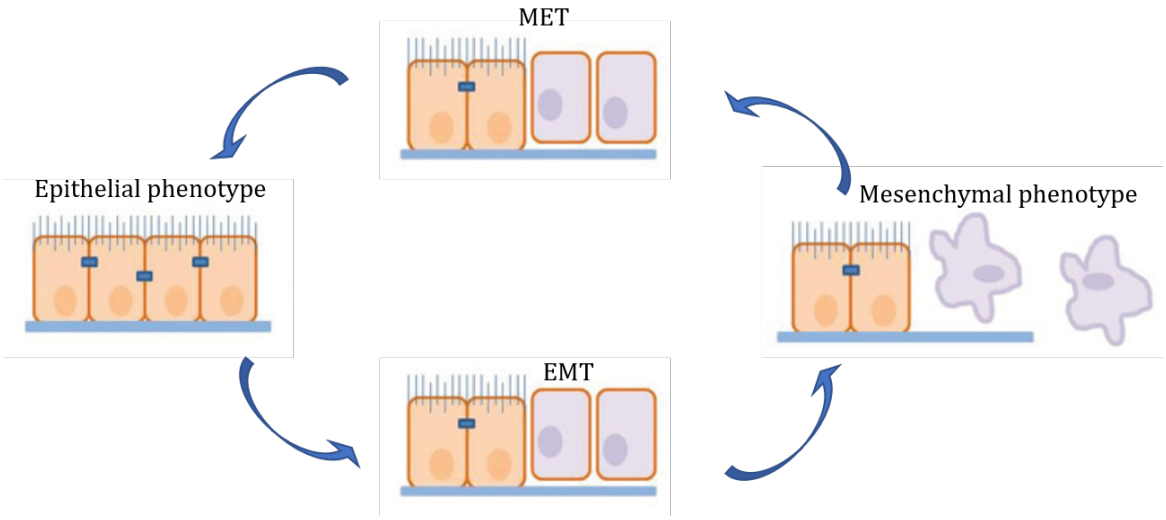

Figure 3.3: Scheme showing the phenotypical changes of tumour cells when they shed into the bloodstream and adhere to a different tissue.

The way that cancer has hitherto been treated consists of removing or killing any damaged tissue using radiotherapy, chemotherapy or surgery. However, more specific and targeted therapies are believed to improve the survival rate. These treatments will be designed to specifically attack each type of tumour cell and will be tailored according to their genetic code. Since they are fragments of the primary tumour cells and therefore have the same DNA, CTCs can provide us with the required information to develop such treatments without a need to perform such expensive or even dangerous biopsies, given that these cells can be obtained through a simple and non invasive blood test [18, 25, 29].

Due to the fact that only 0.1% of the cells shed into the bloodstream by the primary tumour survive, responsible for the even lower concentration of CTCs in a blood test, there are major difficulties to isolate, enumerate and characterise them [25]. Typically between one and ten CTCs among 66106 leukocytes, 26108 platelets and 46109 erythrocytes can be found in a millilitre of blood [10]. Not only does the molecular characterisation of CTCs offer a unique ability to assess genetic features of a cancer, but their counting can also inform about the effectiveness of the treatment: the lower the number of CTCs the greater the effect of the therapy. Unfortunately, most methods in current use are not sensitive enough for reliable enumeration of CTCs in early stage cancer patients [18].

Interestingly, the counting of cells has applications beyond therapies against cancer. For example, the way that pregnancy tests work is based on measuring the concentration in urine or blood of a hormone called human chorionic gonadotropin (hCG). This hormone is released after a fertilised egg attaches to the wall of a woman's uterus. Current devices are not capable of discerning whether a woman is pregnant or not until six days after the fertilisation because of the low initial concentrations of such hormone. As a result, a strong development of cell counting techniques might lead to significant improvements in medical diagnosis and treatments.

3.3 Physical Properties of CTCs vs Lymphocytes

This section aims to summarise comparatively the optical and structural properties of lymphocytes and CTCs in order to asses the behaviour of our plasmonic biosensor. We will fundamentally focus on the refractive index, shape and size for both cell types.

Biological cells can be simply but effectively modelled as a water-based solution with refractive index n_0 and some solids occupying the liquid region within the membrane, mainly proteins. The effective refractive index of the cell, n_{cell} appears to behave linearly with the concentration of protein, according to the empirical expression

$$n_{cell} = n_0 + \alpha C, \tag{3.1}$$

where C is the mass density of protein in grams per decilitre of solution and α the slope of such line, which was found to be $\alpha = (1.845 \pm 0.037) \cdot 10^{-3}$ dLg^{-1} [20]. Despite the presence of lipids and carbohydrates within the cell, which occurs in the form of chemical complexes, it has been investigated that they show similar increments of effective refractive index to proteins, hence the reasonable assumption to include their concentration in C. Similarly,

the effects of temperature, salt and ion concentration seem to show small increments in the effective refractive index. An interesting application of this linear dependence can be found in the diagnosis of anaemia using optical techniques based on the measurement of the erythrocytes' refractive index. Due to their lack of a nucleus and cellular organelles, by obtaining the refractive index of their cytoplasm, the concentration of hemoglobin can be determined as $n_{ery} - n_0 = \beta C_{hem}$, where $n_0 = 1.335$ is the refractive index of cell fluid without hemoglobin and $\beta = 0.0019$ dLg^{-1}. Concentrations below $C_{hem} = 27.4$ gdL^{-1} will be considered as cases of anaemia [20].

There are different types of cells in blood, mainly red blood cells (RBC), white blood cells (WBC) and platelets. RBC are oval biconcave disks without a cell nucleus and rich in hemoglobin. Platelets, which keep the hemostatic equilibrium and prevent blood from clotting, can either have a spherical needle-like structure or a disc-like shape. On the other hand, WBC are the body's main line of defense and can be classified into five types, namely lymphocytes, monocytes, eosinophils, basophils, and neutrophils. Among them, we will focus on lymphocytes since they are the main constituents of the lymphatic system. They have a spherical shape and their diameter is in the range of 6 to 10 μm. Lymphocytes have a relatively simple structure with a huge nucleus that occupies between 70 and 90% of the cell's volume. Their cytoplasmic refractive index was measured to be $n_c = 1.356 \pm 0.002$ refractive index units (RIU) and that of the nucleus $n_n = 1.43 \pm 0.05$ RIU, due to its higher density and protein concentration [20].

Commonly, certain mutations identified in cancer cells show an increased nuclear size, irregular shape and uneven chromatin texture. As a result, their cytoplasmic refractive index can reach values between 1.370 and 1.400 RIU, greater than most healthy cells whose values oscillate between 1.350 and 1.360 RIU. Furthermore, several studies revealed that the nuclear refractive index in tumour cells is increased up to 1.545 RIU, suggesting that this might be an important parameter for cancer diagnosis [20].

The reason why exclusively lymphocytes and CTCs will be compared is because not only can the latter be found in the bloodstream but also in the lymphatic system (lymph). As a result, it is a lot easier to solve the dichotomy between CTCs and lymphocytes than it would be to isolate CTCs in blood, where there is a vast amount of cellular types.

A comparison between WBC, including lymphocytes, and particular CTCs from a colorectal primary tumour (SW-480) can be seen in figure 3.4. As it shows, CTCs are generally bigger and heavier, although their density is lower on average. Despite the already abnormally big nuclear size of CTCs (between 50 and 70% of the cell's volume for this particular cancer [14]), lymphocytes even have greater nuclei, hence their greater compactness and density. It is also noticeable in the graph that this particular type of CTCs exhibit a significantly greater variability of sizes and masses than WBC, despite the fact that these CTCs correspond to a unique type of cell and WBC include five. It shall not be forgotten that tumour cells appear as a consequence of random cell mutations, each of which can have different characteristics, hence their greater standard deviation in volume and mass showed in figure 3.4 and confirmed by the quasi-Gaussian corresponding to tumour cell line SW-480 in figure 3.5, when compared to the volume of WBC. This tendency is, however, not exclusive to this particular cancer cell line and figure 3.5 shows

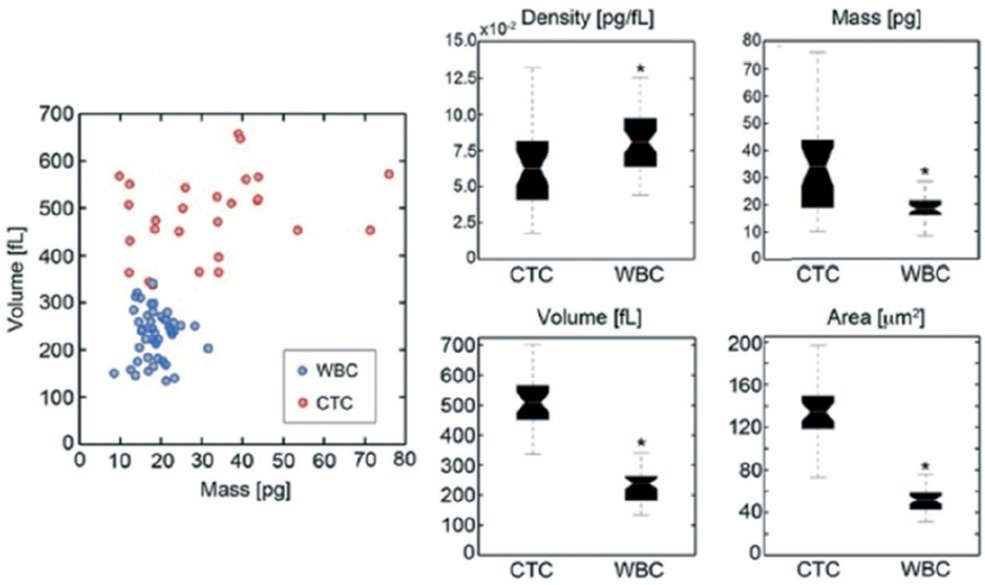

Figure 3.4: Structural properties of WBC compared to those of CTCs from a colorectal primary tumour.

various cases of size distributions wider and centred at greater values than the standard deviation and average size of WBC.

It is worth emphasising in figure 3.5 the average sizes (diameter) of WBC and colorectal SW-480, as well as their standard deviation, i.e. $8 \pm 2\ \mu$m and $11 \pm 4\ \mu$m, respectively. As far as the plasma membrane is concerned, there are very few differences between most eukaryotic cells. As already mentioned, it is formed by a 5 to 10 nm phospholipid bilayer and certain proteins, which result in an overall refractive index of $n_m = 1.50$ RIU.

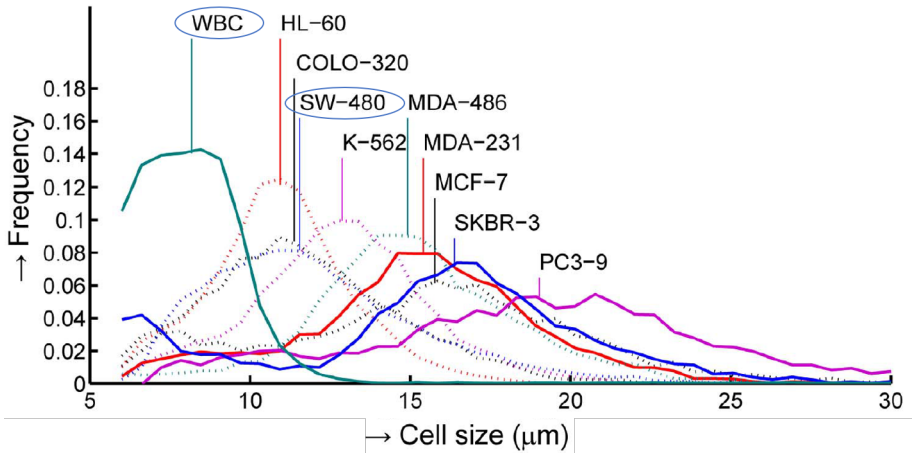

Figure 3.5: Size distribution of WBC and various cancer cell lines, such as prostate cancer PC3-9, colorectal cancer COLO-320 and SW-480, breast cancer SKBR-3, MCF7, MDA-231 and MDA-468.

The most common and efficient way to treat the physics of complex and heterogeneous systems, such as cells, is known as **effective medium theory**. Within this context, a material is called complex if it has several components with a different behaviour concerning the particular property we want to study. As such, the behaviour of the object is dictated by each and every component, that is, its overall macroscopic property is not equal to that of any single constituent, rather it is a collective one contributed by all components forming the system. Therefore, the effective quantity is the equivalent property of a hypothetical simple and homogeneous material with a single component, which yields the same response as that of the complex one at the same conditions [28]. In our case, a cell is a conglomerate of different organelles and other substances, each of them having a different optical behaviour, measured in terms of their refractive index. Throughout this project, cells (lymphocytes and CTCs) are considered as spherical objects with three homogeneous components: membrane, cytoplasm and nucleus. Although more realistic than just a homogeneous sphere with a certain effective refractive index, this model excludes most of organelles in the cell, whose contributions to the overall optical response are included in the refractive index of the main component (out of the three considered) they belong to.

For simple geometries there exist explicit formulas to compute the effective dielectric constant in terms of each homogeneous component's dielectric constant and the volume they occupy [7]. There exist two theories which derive the dielectric function for a medium with spherical inclusions: Maxwell-Garnett and Bruggeman; both of them valid within the small spheres range when compared to the wavelength of light. The expressions for the effective dielectric constant ε_{eff} as a function of the medium's ε_m and the spheres' ε_s are

$$\varepsilon_{eff}^{MG} = \varepsilon_m \frac{\varepsilon_s + 2\varepsilon_m + 2\delta(\varepsilon_s - \varepsilon_m)}{\varepsilon_s + 2\varepsilon_m - 2\delta(\varepsilon_s - \varepsilon_m)}, \tag{3.2}$$

for the Maxwell-Garnett theory, where δ is the volume inclusions-medium ratio, and

$$\delta \frac{\varepsilon_s - \varepsilon_{eff}^B}{\varepsilon_s + \varepsilon_{eff}^B} = (\delta - 1) \frac{\varepsilon_m - \varepsilon_{eff}^B}{\varepsilon_m + \varepsilon_{eff}^B} \tag{3.3}$$

for Bruggeman configuration [24]. Nevertheless, no solutions for the light transmission through the cell and biosensor will be found analytically due to the unapproachable computations needed to solve Maxwell's equations with the boundary conditions imposed by the geometry. As a consequence, numerical methods will be used to solve such partial differential equations in the geometry provided.

Chapter 4

Experimental and Computational Methods

This chapter seeks to provide the reader with a detailed description of the plasmonic biosensor as well as the physical model implemented in COMSOL Multiphysics to calculate the optical response when lymphocytes and CTCs are located on top.

4.1 Golden Nanoholed Plasmonic Device

A golden nanholed array, similar to the one shown in figure 2.3, is used as a biological sensor in order to study the possibility of counting CTCs in a sample of lymph from a patient. The reasons for it to be made of gold are mainly the fact that it is a good metal, which provides the optimal conditions to excite SPPs and EOT, and its advantageous mechanical properties that allow to make thin films. The thickness of the metal plate was chosen to be $t = 60$ nm, as it corresponds to twice the skin depth of SPPs in gold. Due to the fact that the metallic film is placed in the middle of a glass substrate ($n_s = 1.5$) and a liquid buffer, the symmetric and antisymmetric interference modes can couple. For the present study, water is employed as the medium in which cells are immersed, since it shows an equivalent optical behaviour (similar refractive index) to the buffer solutions used to keep the pH constant in biological samples. The holes have a radius of $R = 90$ nm and are periodically perforated with a period $P = 500$ nm in the x and y directions. This periodicity allows the excitation of surface plasmon-Bolch waves in the visible and near infrared range, according to equation 2.10. The nanoapertures are filled with air, following the Cassie and Baxter approach [1], in opposition to Wenzel's configuration in which the holes are filled up with the buffer. Several studies using similar devices confirmed that the liquid forms a line of contact on the rough surface with air trapped below such a line [1]. In other words, the holes are kept dry and no buffer flows through them due to surface tension. Finally, the array is illuminated by a plane wave polarised in the x direction which propagates along the z axis, that is to say, perpendicular to the metal film.

Such a device shows a relatively similar transmission spectrum to the one in figure 2.5, despite the fact that the latter was computed for a two-dimensional geometry. Equivalent

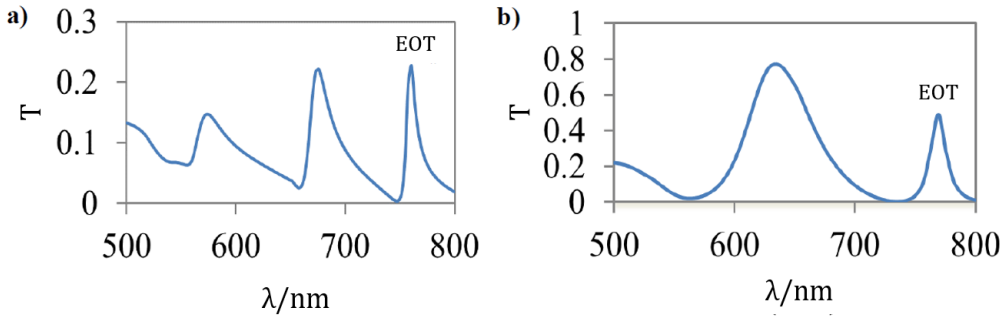

Figure 4.1: Transmission spectra of a periodically nanostructured gold film of thickness $t = 60$ nm and period $P = 500$ nm in between a glass substrate and water. (a) 3D geometry with hole radius $R = 90$ nm, (b) 2D geometry with hole width $W = 180$ nm.

calculations were conducted [6] for the three-dimensional geometry showing an EOT-plasmonic resonance peak at roughly the same wavelength as the 2D simulations, i.e. $\lambda_1 = 769$ nm, as figure 4.1 shows.

When cells are located on top of the gold film, immersed in the buffer, and the whole system is illuminated, the transmission spectrum experiences changes dependent upon the cell's refractive index and geometry. These changes can be evaluated by the shifting of the peaks and the actual transmission value of such maxima. When the maxima shifting is linear with respect to the parameter whose influence we pursue to study, a physical quantity, known as **sensitivity** S_N, can be defined to measure such influence [6]

$$S_N = \frac{\delta \lambda_{max}}{\delta N}, \tag{4.1}$$

where λ_{max} refers to the wavelength of the maximum we focus on and N is that specific parameter, for instance, the cytoplasmic refractive index, the cell's volume immersed within the plasmon penetration region or the degree of contact between the cell and the metal film. This relation existing between the position of the maxima and the optical and structural properties of cells is what can be used to classify an even count them. An increase in the effective refractive index of the material located on top of the metal film (buffer and cells) results, in fact, in the redshift of the peaks.

Extensive research on golden nanoholed devices has recently been undertaken, reporting that, among all the peaks shown in figure 4.1, the EOT maximum, also known as $(1, 0)$ SPP mode, manifests the highest sensitivity to changes in the effective refractive index of the buffer and the material immersed in it [23]. Since the higher the sensitivity, the greater the redshift, an optimal performance of the device is reached when the most sensitive peak is used as biomarker. Consequently, we will exclusively focus on the EOT maximum displacement to classify the cells submerged in the buffer. As explained in chaper 2, this resonance is associated with the excitation of SPPs, which implies that any changes in the effective refractive index further from the sensor than the penetration depth in the buffer ($\delta_d \approx 250$ nm) will not result in the peak displacement. Taking a normal cell diameter of 10 microns into account, only a very small spherical segment of

the cell (of hight 250 nm) has, as a matter of fact, real influence in the peak's shifting. In other words, no changes implemented above 250 nm can be detected by the position of the EOT maximum in this experimental setup.

It is important to consider that cytoeskeletal structures keep the nucleus far enough from the plasma membrane (normally in the centre [14]) to prevent it from potential damages caused by external forces deforming the cell shape. Thus, cellular nuclei will not be detected by the SPP as they are located significantly further from the penetration depth in water and they will not have any influence in the wavelength where the EOT peak occurs. The nucleus has, nonetheless, a pronounced impact on the transmission because of its importantly greater refractive index, which increases the overall effective index. Basically, the presence of cellular nuclei, although does not affect the position of the EOT peak, does decrease its transmittance.

The main purpose of this experimental arrangement is to be able to discern tumour and healthy cells from a liquid and non invasive biopsy, in order to ultimately count them. For such goal we firstly need to attach these cells to the nanostructured surface, for which a microfluidic blood or lymph sample is biofuncionalised using specific molecules such as EpCAM (epithelial cell adhesion molecule) [6]. Under this treatment, cells can get trapped on the biosensor. Later on, by illuminating the sample with a range of wavelengths, measurements of the plasmonic peak shifting and transmittance can be obtained along the sensor. The pairs redshift-transmittance that lay on the tumorous region (after having calibrated the device) will be considered as tumour cells, which can be counted by the number of such pairs.

4.2 Physical Model and Computational Simulations

A numerical approach to the problem is conducted to understand the individual contribution of several physical parameters to the overall functioning of the nanostructured device. All numerical simulations shown in this research have been obtained using COMSOL Multiphysics, based on the finite element method to solve partial differential equations. The three-dimensional problem is computationally difficult to solve, as the number of elements necessary to discretise the system is extremely high. Instead, the two-dimensional version of the sensor-cell system is computed, which shows similar results as several studies previously justified [2, 6]. Particularly, the 2D geometry can be considered as a lower bound of the 3D problem, since the sensitivity has been reported to be higher for the latter. Therefore, every computational result will henceforth represent an underestimation of what should be expected in real conditions.

Despite the vast amount of environments included in COMSOL, only the electromagnetic module will be used to solve this problem. First of all, the geometry needs to be implemented, following the scheme in figure 4.2 a). The whole system, which includes the nanostructured metallic film, the glass substrate, the water buffer and the cell, is periodically repeated each 20 μm using Floquet periodical conditions. Although it would be more accurate, the whole cell immersed in water is not simulated, since such a big area led to unreliable results due to the high number of finite elements. In particular, the

height of the water buffer is 200 nm because it keeps the number of discretised elements low enough to improve numerical convergence and persists with the underestimating tendency, as the penetration depth in water is 250 nm. As a result, the redshift experienced by the EOT peak would still be a lower bound of the expected real value because there are fifty nanometers of buffer and cell within the penetration depth that have not been considered. Having done this, one has to specify the materials for the different components, as well as their dielectric constant, magnetic permeability and electrical conductivity. This structure is illuminated vertically from the substrate with a plane wave polarised along the x axis. Finally, the system is discretised using a mesh with small elements in each of which Maxwell's equations are solved. Consequently, the number of such elements should be as large as possible to obtain more accurate results. The mesh is automatically generated by COMSOL, which increases the number of elements in the most detailed regions.

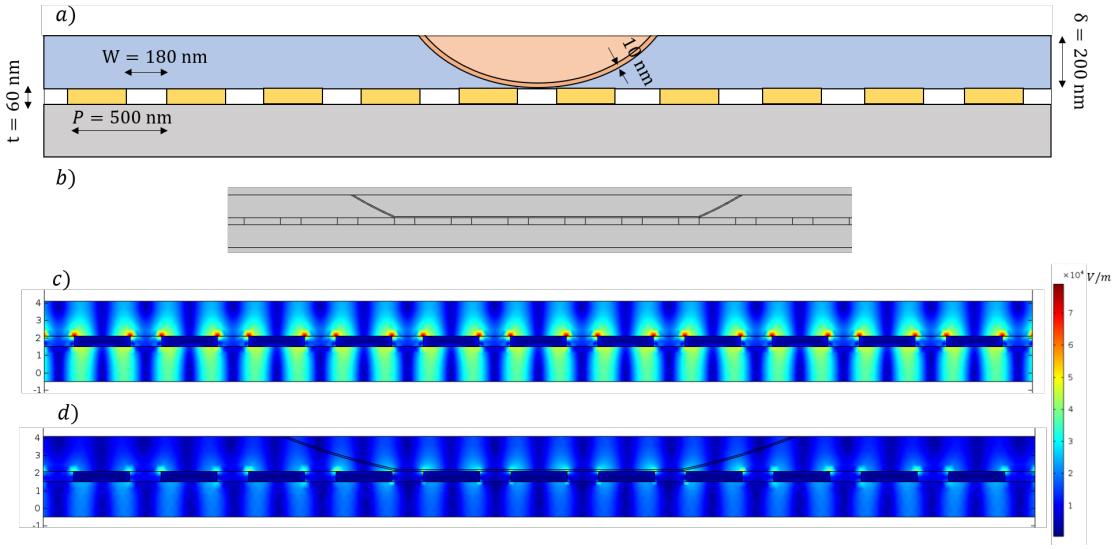

Figure 4.2: a) Scheme of the geometry implemented in COMSOL (cell + buffer + nanostructured gold film + substrate). b) Geometrical implementation showing a cell with flattering 0.4. c) Near electric field of the sensor without cells at the EOT maximum $\lambda_0 = 768.92$ mn and $T_0 = 0.4891$. d) Sensor's near field with a cell of radius $r = 4$ μm, flattering 0.2 and cytoplasmic refractive index $n = 1.356$ at the EOT maximum $\lambda = 769.73$ nm $T = 0.4873$.

There are three geometrical and physical cell parameters, whose influence in the sensor's behaviour are studied, namely cytoplasmic refractive index, cellular radius and its contact with the rough nanostructured surface. It is important to take into account that cells deform when they touch a rigid surface, as they are mainly fluids trapped within the membrane. These changes are dependent upon the cytoskeleton, which keeps a shape as spherical as possible to avoid any nuclear damage. Cells under such deformations are modelled as circles in which a circular segment has been removed, in other words, a cut-off circle by a chord or secant. Furthermore, they will be located in such a way that the circular chord touches completely the sensor surface. We will refer to the length of this chord as contact length. Since the diameter is the maximum chord in a circle, no cells with

a higher contact length than their diameter can be considered using this model. What is more, we will force the limit deformation to be a semicircle, which is an already extreme shape for a cell. Expressed in geometrical terms, the area of the removed circular segment cannot be greater than the remaining truncated circle. Figure 4.2 b) shows an example of these deformations implemented within the whole system. It is important to note that the circular shape is preserved, unlike previous studies [6] where they model such deformations as trapeziums instead of truncated circular segments.

Having fixed the cell radius, a dimensionless quantity known as **flattering** can be defined as the quotient of the contact length divided by the cell diameter. The flattering has the value zero when the cell has not been deformed and the value one for the maximum deformation possible, i.e. a semicircle. Figures 4.2 c) and d) show the near electric field of the sensor with and without a cell at the wavelength of the EOT maximum. It can be noted that the cell in d) has a positive flattering and its presence shifts the peak to the red and decreases the amplitude of the field, hence the transmission goes down.

Previous research has been done on configurations like this one [6], although no cellular structure had hitherto been included, that is to say cells were considered as homogeneous spheres. Basically, Barreda et al. investigated the linear response of the EOT peak shifting under variations of the effective cellular refractive index and the number of holes covered by the cell when it deforms. In this work, a more detailed structure is given to the cell and the influence of each part in the overall plasmonic response is studied. Firstly, we analyse not only the redshift but also the transmittance of the EOT maximum under variations of the cytoplasmic refractive index with and without a cell membrane for two non-deformed cells, corresponding to a lymphocyte and a SW-480 CTC. Secondly, having fixed two cytoplasmic refractive indices corresponding to the two types of non-deformed cells, we analyse the same two properties of the spectrum when the cell radius takes a range of values. More precisely, the redshift and transmittance are studied with respect to the cell's area within the penetration depth. The area of a circular segment can be expressed in terms of the cell radius r as

$$A = \frac{r^2}{2}\left(\theta - \sin\theta\right), \tag{4.2}$$

where $\theta = 2\arccos\left(1 - h/r\right)$ is the maximum angle subtended with respect to the centre of the circle and $h = 200$ nm is the height of the segment submerged in water. Thirdly, the effects of flattering are evaluated for two fixed areas and refractive indices, corresponding to lymphocyte and CTC. The method used to keep the area constant after modifying the flattering consisted of changing the radius of the cell until the area of the deformed cell (computed with a tool provided by COMSOL) matched the area of the non-deformed.

In order to obtain a more realistic understanding of how the sensor could be used to discern between healthy and cancerous cells, two samples of 50 cells with different values of cytoplasmic refractive index, flattering and cell radius are simulated. The membrane is supposed to present negligible dissimilarities from one cell to another, thus it is considered equal in all cases. One sample corresponds to lymphocytes and the other to colorectal SW-480 CTC. A Gaussian distribution of values for each parameter is considered, according

to bibliographical results [10, 20]. As far as the flattering is concerned, we could not find any biological studies that reported how cells deform when they come into contact with surfaces in terms of the flattering or similar quantities. As a result, we assume that every possible flattering between zero and one is equally probable, hence the use of a uniform distribution. Table 4.1 shows all the parameters considered as well as their distributions.

Physical Quantity	**Distribution**	**Lymphocyte**	**SW-480 CTC**
Diameter, $2r$ (μm)	G	8 ± 2	11 ± 4
Flattering	U[0,1]	-	-
Cytplasmic index, n (RIU)	G	1.356 ± 0.002	1.380 ± 0.002
Membrane index, n_m (RIU)	-	1.5	1.5
Nuclear index, n_n (RIU)	G	1.43 ± 0.03	1.543 ± 0.002
Relative nuclear radius, r_n (%)	G	80 ± 10	60 ± 10

Table 4.1: Physical parameters introduced in the model for both cell types involved and their distribution, where G stands for Gaussian and U[0,1] uniform in the interval [0,1].

As might have been noted, no attention to the nucleus has been paid yet. Despite its negligible influence in the peak shifting, because its distance to the membrane is greater than the penetration depth, it is an important factor in the transmission. The nucleus is the cellular component with greatest refractive index and can increase significantly the effective index of the whole cell if it is taken into account. The transmittance between a dielectric surface with index n_{eff} and water at normal incidence is given by the equation

$$T = 4\frac{1.33 \cdot n_{eff}}{(n_{eff} + 1.33)^2}, \tag{4.3}$$

which implies that for $n_{eff} > 1.33$, as it is the case, the greater the effective index of the cell the lower the transmission of light from the cell to the buffer, as shown in figure 4.3.

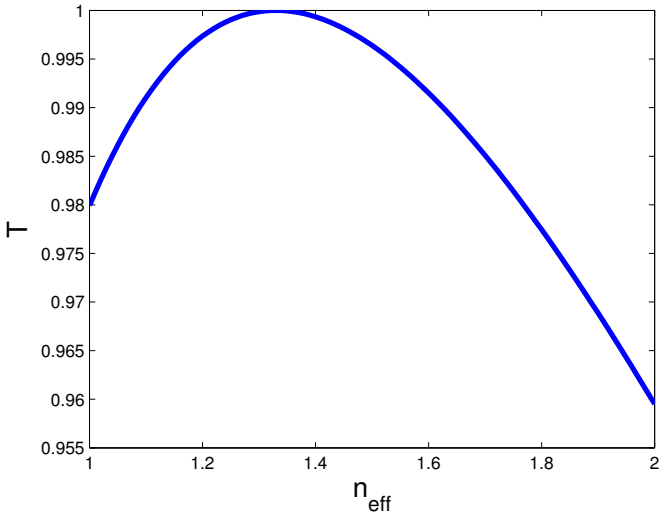

Figure 4.3: Transmittance dielectric-water at normal incidence vs dielectric's index.

As a consequence of the nucleus, less light is transmitted through the buffer and even less trough the whole system, resulting in a generalised reduction of transmission in the spectrum. Ideally, the way to model this factor would be by increasing the area dedicated to the buffer and cells, so that the nucleus can be included. However, this model requires a much greater mesh to be solved, leading to non-convergent computational results. Instead, the nuclear influence in transmittance is treated separately from the already considered small part of cell immersed in water and located on top of the biosensor.

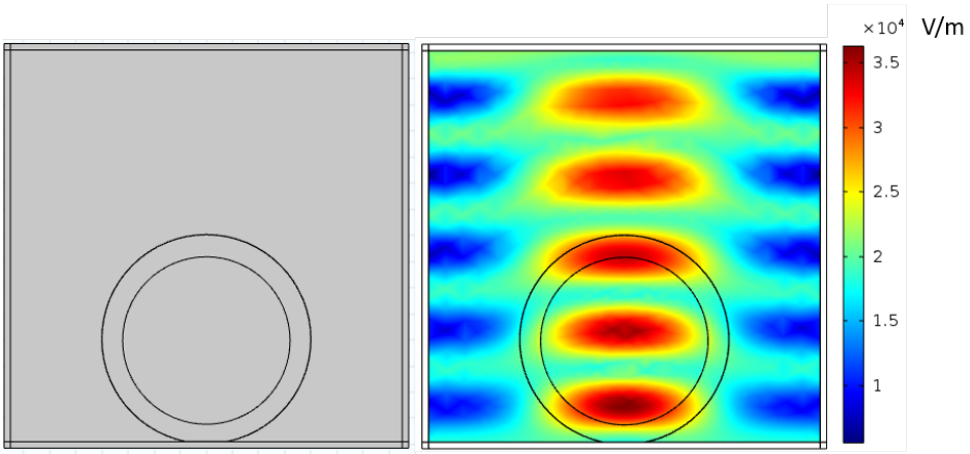

Figure 4.4: Geometrical scheme and near electric field at $\lambda = 769.73$ nm of the nuclear physical model showing a cell of radius $r = 4$ μm, relative nuclear radius $r_n = 80\%$, flattering 0.2, cytoplasmic refractive index $n = 1.356$ and nuclear index $n_n = 1.43$.

The nuclear physical model consists of a 20-μm-side square made of water, where cells are located at the bottom. In this case the whole cell is included with the same geometrical features as before, i.e. membrane, cytoplasm and flattering, plus the nucleus. Figure 4.4 illustrates an example of this implementation, in which the nucleus is considered as a perfect circle. The nuclear radius is introduced as a percentage of the cell's that oscillates between 70% and 90% for lymphocytes, and 50-70% for CTCs. As previously, the system is illuminated vertically from the bottom with a plane wave polarised in the x direction. The reason why COMSOL offers reliable results in this case, despite its greater size, is the lower level of detail compared to the nanostructured gold film.

There are three properties of the nucleus we want to study: nuclear radius, nuclear refractive index and nuclear positioning. Having fixed the cellular size and cytoplasmic index, the transmittance of the system is measured for the wavelength corresponding to the EOT maximum computed with the first configuration. According to this procedure, we analyse the individual effect of the nuclear index and radius to transmission. It is worth taking into account that nuclei are mainly located in the centre of cells, although their position shows significant changes during mitosis [14]. Therefore, a study of the transmission under horizontal and vertical variations in the location of the nucleus is also conducted.

The final contribution of this research is to find the collective contribution from both models with the same two samples of 50 healthy and tumour cells previously considered.

The values of nuclear radii and refractive indices are shown in table 4.1. Furthermore, the nucleus is randomly located in different parts of the cell surrounding the centre . For each of the hundred cases a random number for every parameter in table 4.1 is generated using the corresponding distribution. The cytoplasmic index, flattering and radius are introduced in the model including the sensor and the position λ of the peak is determined. That wavelength is implemented in the nuclear model together with the relative nuclear radius and refractive index, for which the transmittance T is computed. Since the circular segment of cell, used in the first model, contributes insignificantly to the reduction of transmittance, this quantity will be taken from the transmission computations using the second, but scaled with the transmittance of the EOT peak when the sensor has no cells on top ($T_0 = 0.4891$). The redshift caused by the cell is measured using the position of the plasmonic maximum in the first model. In other words, the transmittance increment is calculated as $\Delta T = T \cdot T_0 - T_0$, and the redshift $\Delta\lambda = \lambda - \lambda_0$. The former is expected to be a negative number and the latter positive, since cells cause a positive displacement of the plasmonic peak and decrease its transmittance.

Having computed these two quantities, a map ΔT vs $\Delta\lambda$ can be created. The positions of lymphocytes and CTCs in this map provide the experiementer with a guideline to determine whether a cell is healthy or not by the region of the map on which the spectral properties of that cell lay. As a result, among the cells adhered to the sensor, one can easily count the cancerous ones.

Chapter 5

Results and Analysis

In this chapter the main results of this research are shown. Initially, we present the individual contribution of the main cellular components using the first physical model including the nanostructured surface. Secondly, this model is used to simulate two realistic samples of 50 healthy and cancerous cells. Thirdly, the influence of the nucleus is reported using the nuclear model. Lastly, a map showing the redshift and transmittance change for the two previous random samples is displayed, in which the analysis from both physical models has been incorporated.

5.1 Membrane and Cytoplasmic Refractive Index

Let us consider two non-deformed cells, representing a lymphocyte and a CTC with radii 4 and 7 μm, respectively. Following the geometry in figure 4.2 a), we study the maximum wavelength and transmittance of the EOT peak for eight different cytoplasmic refractive indices with and without a 10 nm thick plasma membrane of index $n_m = 1.5$. Thirty two different spectra were analysed, showing the behaviour represented in the small subfigure in 5.1 for increasing indices. Figure 5.1 shows the wavelength and transmittance at maxima for the eight indices considered. There exists a linear dependence of such wavelength with the cytoplasmic index, whose sensitivities are $S_n^{lym} = 25.13$ and $S_n^{CTC} = 35.3$ nm/RIU, in agreement with the calculations performed by Barreda et al. [6], who studied cells of radius 10 μm and reported a sensitivity of 47.1 nm/RIU. Transmission, however, does not follow that linear tendency, but it depends quadratically on the cytoplasmic index.

As far as the plasma membrane is concerned, no difference can be detected in the sensitivity to cytoplasmic refractive index, as the lines with and without membrane are parallel for both the lymphocyte and CTC. The effect of membrane is an overall increase of the effective refractive index that shifts the maximum a few tenths of manometer. This shift can be measured as the difference between the y-intercepts of the parallel lines. Interestingly, its value for the lymphocyte is 0.25 nm and for the CTC 0.45 nm, due to the greater radius of the latter, which results in a greater portion of membrane within the simulated height of buffer and a greater effective index. This wavelength shifts seem to be proportional to the displacement that the quadratic curves of transmittance experience when the membrane is included.

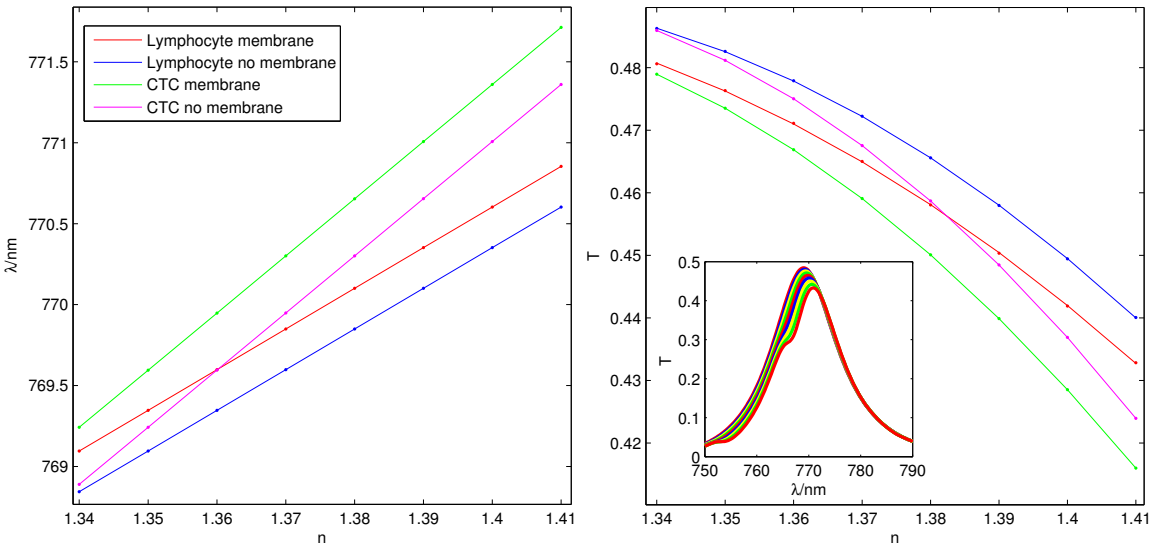

Figure 5.1: Wavelength and transmittance at the EOT maximum vs cytoplasmic refractive index for a lymphocyte and a CTC of radii 4 and 7 μm with and without a membrane. The fits are linear for λ and quadratic for T. Subfigure shows the EOT peak for the eight computations of the lymphocyte with a membrane.

As expected, the wavelength at maximum and its transmittance have inversely proportional behaviours when the effective index increases. Furthermore, the slopes are greater for the biggest cell, as there is a bigger area of buffer occupied by a different object with higher index and the effective index of the system buffer+cell increases. Therefore there is an influence of the portion of cell submerged in water on the transmission spectrum, which is studied in the following section. From now on every simulated cell will include a plasma membrane of thickness 10 nm and refractive index 1.5.

5.2 Radius and Immersed Cell Area

Let us now consider two non-deformed cells with fixed cytoplasmic indices 1.356 and 1.380, representing a lymphocyte and CTC, respectively. In this occasion the radius takes a range of values between one and eight microns and we study how the wavelength and transmittance at the plasmonic maximum change when the cell area immersed within the 200 nm of water increases. According to equation 4.2, such area can be directly computed from the cell radius.

As figure 5.2 illustrates, there exists a linear behaviour of the wavelength and transmittance with the area of cell immersed within the water buffer and their tendencies are inversely proportional. The reason for this is similar to the previous case, that is to say, the greater the area of the cell, the higher the effective refractive index of the system cell+buffer. Curiously, transmittance does not decrease quadratically with the area as it does with the cytoplasmic index. Sensitivities to submerged area are $S_A^{lym} = 1.3531$

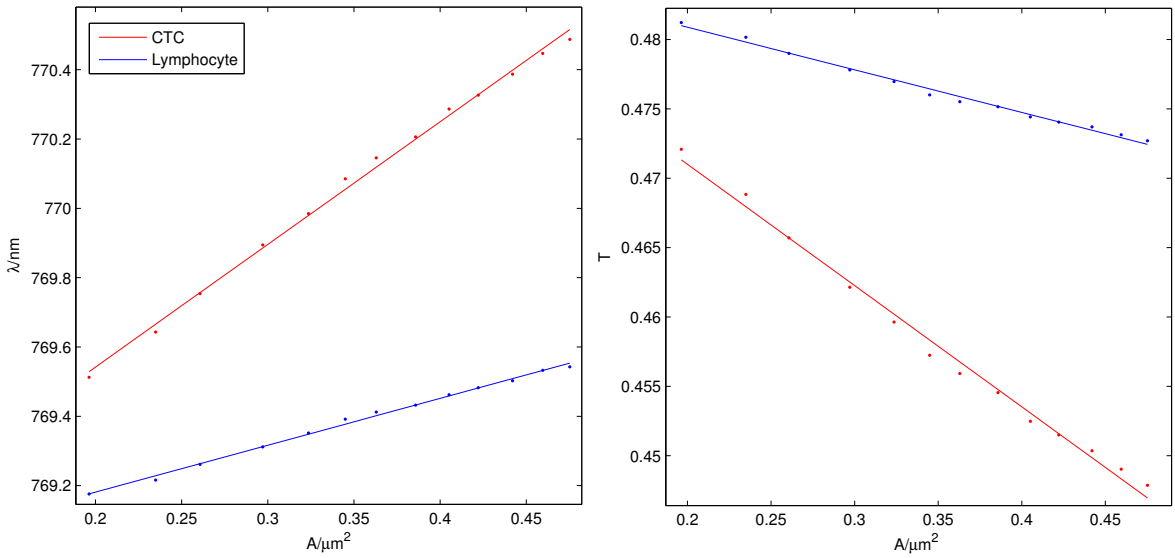

Figure 5.2: Wavelength and transmittance at the EOT maximum vs cell area immersed within the water buffer for a lymphocyte and CTC with cytoplasmic indices 1.356 and 1.380. The fits are linear for both λ and T.

and $S_A^{CTC} = 3.5386$ nmμm^{-2} and the slopes of transmittance $\alpha_A^{lym} = -0.0307$ and $\alpha_A^{CTC} = -0.0874$ μm^{-2}. In comparison with sensitivities to cytoplasmic index, the position of the EOT maximum seems less strongly dependent on the submerged area than on the cell's effective index. Particularly, the two cells considered in the previous section had an immersed area of 0.335 and 0.444 μm^2, a factor 1.33 between areas that provokes a factor 1.40 between sensitivities to cytoplasmic index. In this case, lymphocyte and CTC differ in just three hundredths of cytoplasmic index and the sensitivity to area increases in factor 2.6.

If figures 5.1 and 5.2 are compared, it can be noted that the fits in the former are in much greater a agreement with the simulated results than those in the latter. Since no experimental inaccuracies can excuse this deviation, an explanation can be given in terms of geometry. The effect of cytoplasmic index was conducted with two cells whose shape did not change at all during the increase of index. Nevertheless, when the area was changed, distances from some points of the cell to the film slightly did as well, resulting in a small deviation from the linear behaviour imposed by the change of radius. Mathematically, both wavelength and transmittance at the maximum can be expressed as

$$\begin{cases} \lambda = b_1 + S_A \cdot A + \mathcal{O}(A^2) \\ T = b_2 + \alpha_A \cdot A + \mathcal{O}(A^2), \end{cases} \tag{5.1}$$

where b_i are the corresponding $y-$intercepts and $\mathcal{O}(A^2)$ a polynomial of degree strictly greater than one that represents the geometrical factor causing such small deviations from the linear behaviour.

5.3 Flattering

In this section we study the effect of flattering in a lymphocyte and SW-480 CTC with fixed cytoplasmic indices ($n^{lym} = 1.356$, $n^{CTC} = 1.380$). The cell area immersed in water is kept constant while flattering increases from zero to one, that is to say, from a point of contact to a diameter. The area of the region within the buffer was initially fixed as 0.8 μm^2 for both lymphocyte and CTC, which corresponds to a non-deformed cell of radius 23 μm, according to equation 4.2. The reason why such a big cell was considered is because the radius had to be progressively reduced as flattering increased, as more contact length leads to a larger area within the 200 nm of water. In particular, in order to preserve the same area for the maximum flattering, a cell of radius 2 μm was needed. Figure 5.3 shows the two extreme cases of flattering for cells with the same area immersed in water.

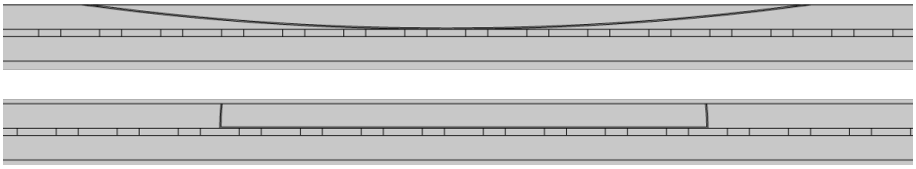

Figure 5.3: Two cells with flattering zero (above) and one (below) having the same area inside the buffer (0.8 μm^2). Their radii are 23 and 2 μm, respectively.

Following this reasoning, wavelength and transmittance at the peak are plotted against flattering for the two cytoplasmic indices. As presented in figure 5.4, both quantities depend linearly on flattering, with sensitivities $S^{lym}_{flat} = 0.3425$ nm and $S^{CTC}_{flat} = 0.707$ nm. The slopes of transmittance lines are $\alpha^{lym}_{flat} = -0.0084$ and $\alpha^{lym}_{flat} = -0.0208$.

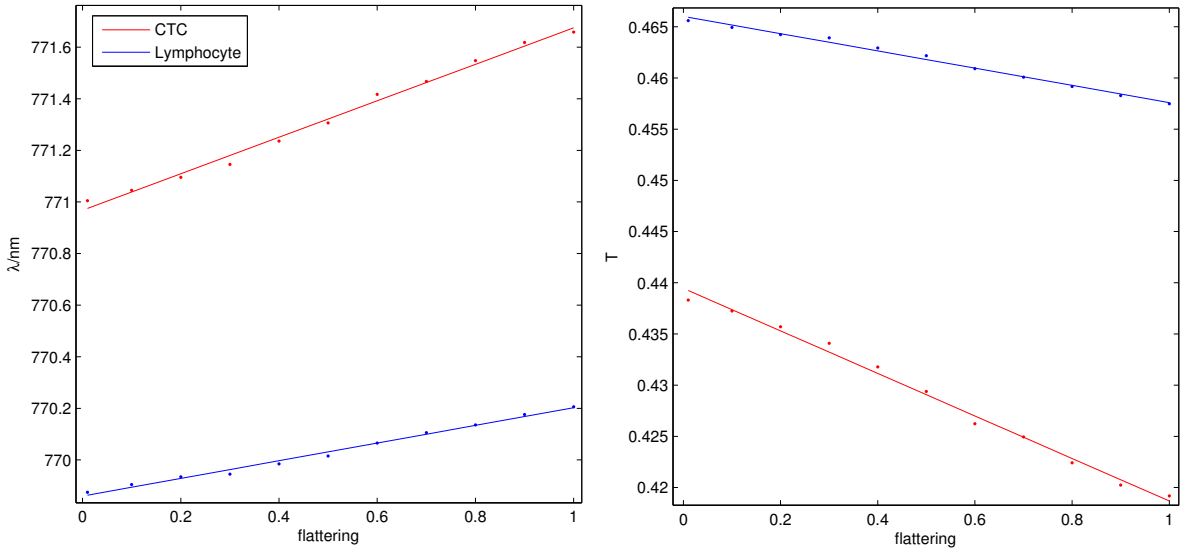

Figure 5.4: Wavelength and transmittance at the EOT peak vs flattering for a lymphocyte and CTC with cytoplasmic indices 1.356 and 1.380 and same area inside the buffer.

Barreda et al. studied the influence of object deformations but they focused on the amount of holes blocked by such object and reported a sensitivity of 0.21 nm per nanoaperture for a cell of radius 10 μm, in agreement with our results [6]. However, we shall specify that it is the contact length and not the number of apertures blocked by the cell what causes a linear redshift of the peak. Due to the fact that only a new pair of holes were completely blocked when the flattering was 0.2, 0.4, 0.7 and 1, finishing with eight completely covered apertures, if Barreda's hypothesis were true, the wavelength plot would present four steps at the previous values, each of which representing a new set of blocked holes. On the contrary, there is a smooth progression of the results, which show increasing redshift and transmittance even when no new apertures have been covered. As a result, we can conclude that both wavelength and transmittance at the plasmonic peak behave linearly with the contact length of the cell.

As discussed earlier, greater effective indices yield more significant spectral changes and the higher sensitivity to flattering when the cytoplasmic index is 1.380, compared to the case when $n = 1.356$, confirms such statement. The small deviations of the simulated results from the linear fit can be again justified by the geometric factor explained in the previous section. In this case, if f represent the flattering, a polynomial of degree greater than one in the variable f, $\mathcal{O}(f^2)$, represents such factor.

5.4 A First Realistic Approach

Let us now consider two samples of 50 lymphocytes and SW-480 CTCs. Their radii are modelled with a Gaussian centred at 4 and 5.5 μm, and standard deviations 1 and 2 μm. Cytoplasmic refractive indices also follow a normal distribution of means 1.356 and 1.380, and widths 0.002. Finally, both cells are supposed to have equally probable values of flattering, thus represented by a uniform distribution. Three random numbers for each cell are generated according to these distributions. After having simulated both samples and focused on the plasmonic peak, the change in transmittance $\Delta T = T - T_0$ is plotted against its redshift $\Delta\lambda = \lambda - \lambda_0$ in figure 5.5, where $T_0 = 0.4891$ and $\lambda_0 = 768.92$ nm.

One could expect that the randomisation of the three apparently independent variables would result in a cloud of uncorrelated points. On the contrary, figure 5.5 shows two sets of 50 points that fit perfectly to a pair of lines, whose slopes are -0.024 and -0.027 nm^{-1} for lymphocytes and CTCs, respectively. Let us analyse the contribution of the three already studied parameters in order to understand such unexpected behaviour. According to the previous sections, both wavelength and transmittance depend linearly on the flattering f, immersed area A and cytoplasmic refractive index n, except for the transmittance with respect to the latter, whose dependence is quadratic. All this can be summarised in the following equations.

$$\begin{cases} \lambda(n) = a_n \cdot n + b_n \\ \lambda(A) = a_A \cdot A + b_A \\ \lambda(f) = a_f \cdot f + b_f \end{cases} \quad \begin{cases} T(n) = \alpha_n \cdot n^2 + \beta_n \cdot n + \gamma_n \\ T(A) = \alpha_A \cdot A + \beta_A \\ T(f) = \alpha_f \cdot f + \beta_f, \end{cases} \tag{5.2}$$

where $a_i, b_i, \alpha_i, \beta_i$ and γ_n are constants with respect to the parameter $i \in \{n, A, f\}$.

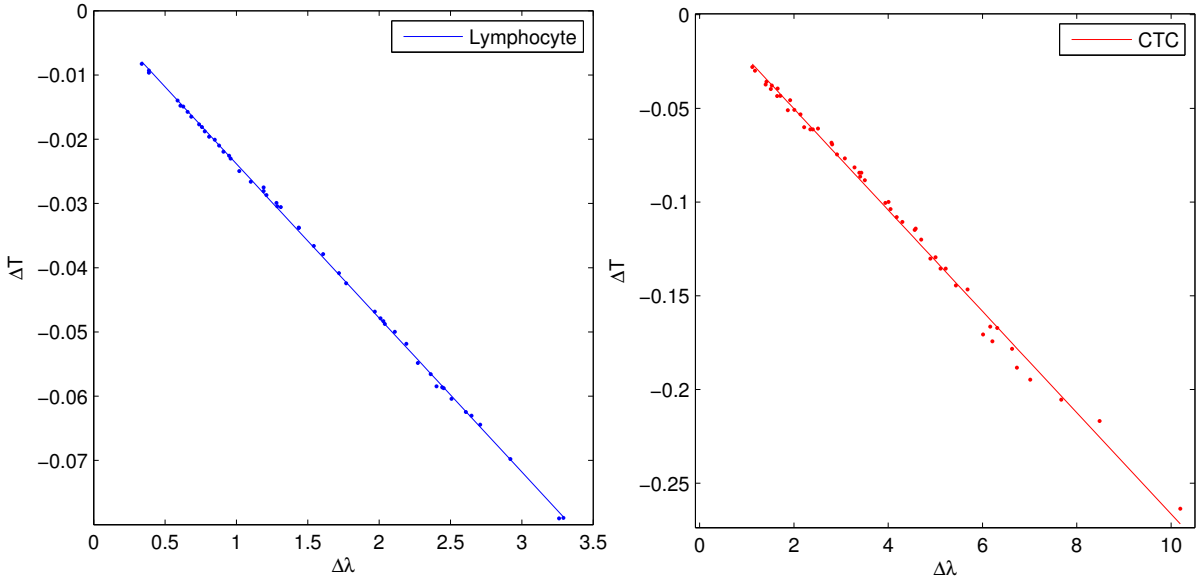

Figure 5.5: Transmittance change $\Delta T = T - T_0$ vs redshift $\Delta\lambda = \lambda - \lambda_0$ for two samples of 50 lymphocytes (left) and 50 SW-480 CTCs (right).

From the system of equations in 5.2, one can easily infer a linear dependence of T with respect to λ, by combining the λ and T equations for the parameters A and f. However, the same two equations in terms of n lead to a quadratic dependence of T with respect to λ. Despite this seemingly contradictory statement, our results are perfectly coherent, as $a_i, b_i, \alpha_i, \beta_i$ are constants with respect to parameter i but not with respect to the others. For instance, a_n is constant for n at the same time as a function of A and f, i.e. $a_n = a_n(A, f)$. Therefore, the first transmittance equation can be rewritten as

$$T(n, A, f) = \alpha_n(A, f) \cdot n^2 + \beta_n(A, f) \cdot n + \gamma_n(A, f). \tag{5.3}$$

Taking into account the fact that the standard deviation of the Gaussians representing the distribution of n for both samples was barely 0.002, we can assume that the cytoplasmic refractive index remains almost constant for the 50 cells in the sample. In other words, the range of values in which the cytoplasmic index is allowed to be is a lot smaller than for the other two parameters. As a result, n can be considered as a constant in equation 5.3 and T would only be a function of A and f, leading to the linear behaviour obtained computationally and shown in figure 5.5. As a matter of fact, this model would predict a steeper slope for greater cytoplasmic indices, which is exactly what we present, as the slope for CTCs ($n \sim 1.380$) is three thousands greater in absolute value than for lymphocytes ($n \sim 1.356$). We thereby confirm a linear correlation of the transmittance and wavelength at the EOT maximum when only the part of the cell within the penetration depth is considered.

This result is, nevertheless, not fully realistic, as only a tiny part of the cell has been taken into account. Although irrelevant to the plasmonic peak position for being above

the penetration depth, the remaining cell portion plays a fundamental role in the overall transmission, as it breaks the commented correlation between λ and T. Particularly, nuclei are the main contributors to such effect.

5.5 Nucleus

In this section the nuclear model is used in order to analyse the transmission of light through the entire cell. There are three properties of the nucleus we focus on, namely its refractive index, size and position within the cell. All simulations were performed with a non-deformed cell of radius 4 μm and cytoplasmic index 1.356. Transmittance was computed for the wavelength of the EOT maximum corresponding to this parameters ($\lambda = 769.31$ nm).

5.5.1 Nuclear Refractive Index

In this occasion the influence of the nuclear refractive index is reviewed. The nucleus is located in the centre of the cell and three different relative nuclear radii ($r_n = 60, 70, 80\%$) have been simulated, which represent the most typical values for the two types of cell considered throughout this research.

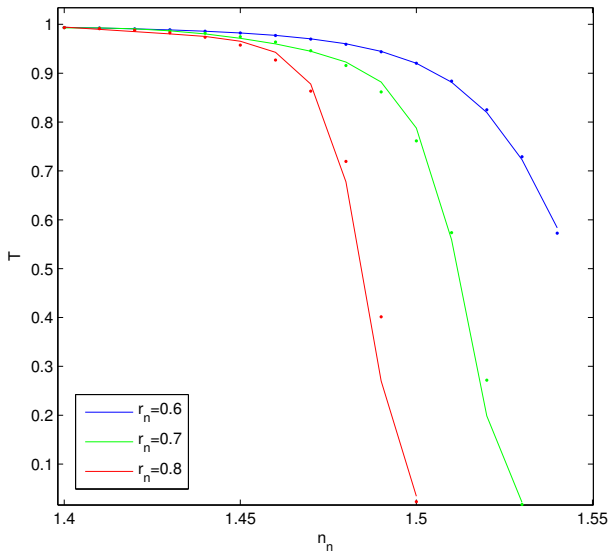

Figure 5.6: Transmittance through the cell vs nuclear refractive index at the wavelength $\lambda = 769.31$ nm for three nuclear relative radii.

In figure 5.6 transmittance against nuclear index is plotted, which seems to follow a negative exponential growth. The best fits for the three relative radii were found with a curve of the form $T = \left(1 + e^{An_n^2 + Bn_n + C}\right)^{-1}$, where A, B and C are real fitting parameters. As can be also inferred from the figure above, transmittance is systematically lower for grater nuclear sizes, since the effective cellular index increases with n_n. The interval

of nuclear indices was chosen to be $[1.40, 1.55]$ as it includes the values for lymphocytes ($n_n = 1.43$) and SW-480 CTCs ($n_n = 1.54$) [10]. It is worth mentioning that lymphocytes, whose nuclear radii represent an 80% of the cell's, exhibit values of transmittance close to one, as the red curve shows. On the other hand, SW-480 CTCs, with relative radii of 60%, can experience a huge variation of transmittance, depending on the width of the nuclear radii distribution. As commented before, refractive indices (both nuclear and cytoplasmic) are very well determined properties that present much lower variations than other cell parameters like the size.

5.5.2 Nuclear Size

As demonstrated in the previous paragraphs, there exists a strong dependence of transmittance with the nuclear relative radius. Figure 5.7 shows such dependence for a nucleus located in the centre of the cell. We particularly wanted to pay special attention to big nuclei, since this is the case for all the cells we are considering. As a consequence, relatively low nuclear indices had to be considered in order to avoid a quick convergence to zero transmission. This results in a study of the nuclear size potentially more focused on lymphocyte-like cells, as the indices considered oscillate between 1.43 and 1.46.

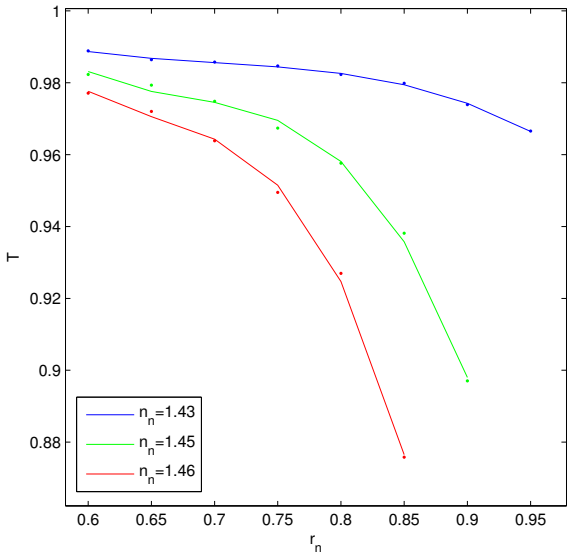

Figure 5.7: Transmittance through the cell vs nuclear relative radius at the wavelength $\lambda = 769.31$ nm for three nuclear refractive indices.

The figure above shows a strong reduction of transmittance that sharpens significantly for greater nuclear indices. Unlike in figure 5.6, transmittance follows a polynomial decrease with the radius rather than exponential. The three curves were fitted to a polynomial in r_n of degree three, which seems too model the transmittance behaviour for low nuclear index. Comparatively with respect to CTCs, lymphocytes exhibit a much smaller range of transmittance values, as their nuclear index can go from 1.40 to 1.46 and their

relative nuclear radius from 0.7 to 0.85 or 0.9 (two Gaussians centred at 1.43 and 0.8, respectively) [20]. Figure 5.7 confirms that the interval of possible transmittance values for lymphocytes is [0.70, 0.98], in contrast to CTCs, whose range is [0.30,0.97], as their nuclear index varies from 1.541 to 1.545 and nuclear relative radius from 0.5 to 0.7 [20]. This larger transmittance spreading will play a fundamental role in CTC detection and enumeration.

5.5.3 Nuclear Positioning

The last nuclear property to be examined in this research is the influence of its location within the cell. Essentially, the nucleus was moved in the vertical and horizontal directions to compute the transmittance through the same cell of radius 4 μm, cytoplasmic index $n = 1.356$ and nuclear index $n_n = 1.43$, in which the nuclear relative radius took values from 0.6 to 0.8. Let us place 13 equispaced points laying on the vertical diameter of the cell, in such a way that there are 12 equally distanced divisions of such diameter and two extreme parts of length equal to the nuclear radius. This configuration leads to 13 possible positions for the centre of the nucleus, in which the two closest to the cell limits make the nucleus be tangent to the inner part of the membrane. Coordinate ξ refers to the vertical position of the centre of nucleus with value zero when the nucleus is tangent to the bottom of the cell and value one when it is tangent to the top. Similarly, this partition is performed in the horizontal diameter and η is the coordinate whose value is -1 when the nucleus is tangent to the left side of the cell and 1 when it is to the right side. Figure 5.8 shows the transmittance against these two nuclear coordinates.

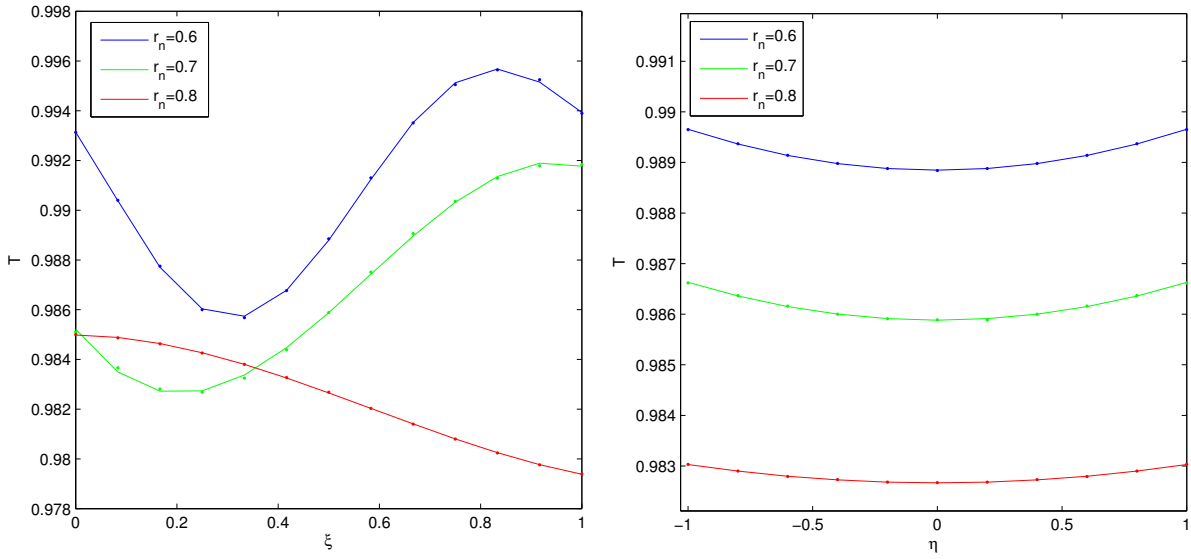

Figure 5.8: Transmittance through the cell vs nuclear position in the vertical (left) and horizontal (right) ξ, η coordinates at the wavelength $\lambda = 769.31$ nm for three nuclear relative radius.

As can be inferred from both graphs, the influence of the nuclear position is not as significant as the other two nuclear properties, at least for the three nuclear relative radii considered. In both directions of nuclear motion, the maximum transmittance variation was reported to be less than 0.01, as can be found in the blue curve for the vertical direction. A general tendency is the greater level of difference in light transmission with the nuclear motion for decreasing radii, as the blue curves show in comparison with the other two. As the nuclear size grows, less space inside the cell can be occupied and less prominent movements can take place. Interestingly, between 0 and 0.35 units in the ξ coordinate, a higher transmission is observed for $r_n = 0.8$ than $r_n = 0.7$, despite the lower effective index of the latter. What is more, the red curve shows a maximum in that region when the other two present a minimum. An explanation to such surprising phenomenon can be given in terms of the lensing effect of the nucleus when it is close to the bottom of the cell for that radius, which overcomes its higher refractive index and transmits more light than a cell with $r_n = 0.7$.

As can be expected from the geometry, transmittance is symmetrical with respect to the vertical line crossing the origin of the η coordinate. Furthermore, a quadratic fit in η is seemingly the best one for those three curves. Regarding the vertical motion, maximum transmittance for relative radii between 0.6 and 0.7 is found for positions of the nucleus close to the top of the cell. These curves present a polynomial behaviour and were fitted to cubics.

5.6 A Second Realistic Approach

The following paragraphs aim to collect the individual contribution from preceding sections in order to evaluate the accuracy of our biosensor in the discernment between lymphocytes and SW-480 circulating tumour cells. It is worth mentioning, that the same procedure could be conducted for different cellular lines, after having adjusted the physical parameters involved in our two geometrical implementations. During this collective study, simulations are conducted with the same parameters used throughout the previous studies and summarised in table 4.1.

In first place, the same two samples of 50 lymphocytes and CTCs from section 5.4 were considered. For each cell, two new random numbers were generated for the nuclear relative radius and refractive index. For the value of the wavelength at the EOT maximum, transmittance through the entire cell is computed using the nuclear model.

In order to plot a graph showing the transmission change of the EOT maximum against its redshift, we need to consider a unique value for each cell's transmittance. Accounting for the the fact that the two physical models showed two different transmittances for only one value of wavelength, a combination of the two was used for the map ΔT vs $\Delta\lambda$. Since values of transmittance above $T_0 = 0.4891$ do not make any sense, as a cell located on top of the gold film necessarily decreases the amplitude of the peak, the transmittance computed with the nuclear model was scaled by this factor T_0. In other words, if T is the value of transmittance computed with the nuclear model, $\Delta T = T \cdot T_0 - T_0$. Transmission from the first model was dismissed and only the scaling factor from the empty sensor was

taken into account, mainly because we wanted to break the unrealistic and non-intuitive correlation given by a model that considers, exclusively, a very small part of the cell inside the plasmon's penetration depth. Figure 5.9 shows this transmittance change against redshift for both samples of 50 healthy and tumorous cells.

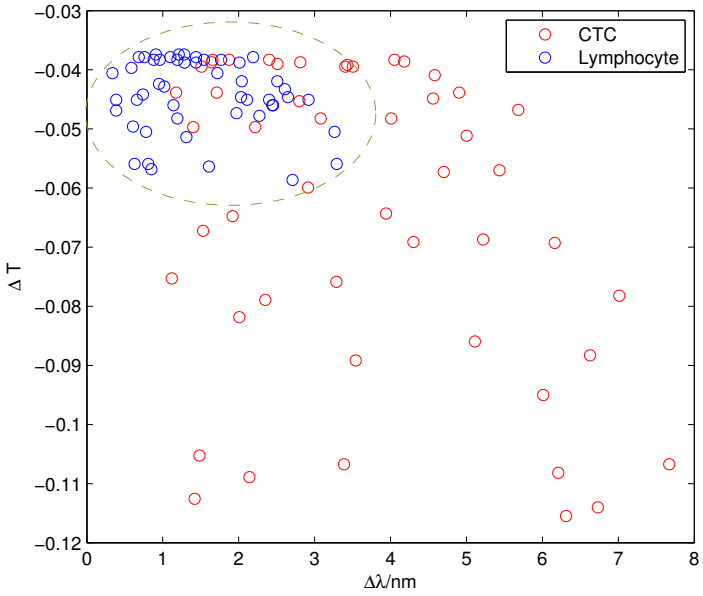

Figure 5.9: Transmittance change vs redshift computed for two samples of 50 lymphocytes and SW-480 CTCs

As figure 5.9 shows, lymphocytes present much lower and less dispersed transmittance changes and redshifts, because of their generally lower sizes, cytoplasmic and nuclear refractive indices, compared to CTCs. According to the graph, only a restricted portion corresponds to the spectral properties of the EOT peak for lymphocytes, whereas CTCs are significantly more widespread along the map. The average redshift and transmittance for lymphocytes are $\langle \Delta\lambda \rangle^{lym} = 1.51$ nm and $\langle \Delta T \rangle^{lym} = -0.044$, whereas for CTCs $\langle \Delta\lambda \rangle^{CTC} = 3.65$ nm and $\langle \Delta T \rangle^{CTC} = -0.064$. Their standard deviations are $\sigma_{\lambda}^{lym} = 0.80$ nm and $\sigma_{T}^{lym} = 0.006$ for lymphocytes and $\sigma_{\lambda}^{CTC} = 1.80$ nm and $\sigma_{T}^{CTC} = 0.026$ for cancer cells. As shown by the oval region representing the location for lymphocytes, there are 17 out of the 50 CTCs simulated laying within the dotted curve. This implies that the probability of determining whether a cell in the lymph is cancerous our not using this experimental setup is 66%, as we would not be able to distinguish between a lymphocyte and a CTC that appears inside the dashed area.

Considering the fact that two-dimensional simulations were conducted and both models have been design to contribute to the underestimating tendency, this 66% is only a lower bound of the real accuracy for this diagnostic tool. By using a more realistic three-dimensional model, cells would spread out and less CTCs would appear inside the dotted region, increasing the device's reliability in CTC detection. Furthermore, there exists a strong likelihood that a model including the metal film and the whole cell will cause

a greater reduction in the transmittance of the peak. Unfortunately, COMSOL is not powerful enough to perform such task and we have to reluctantly accept the combination of two models, which is supposed to give underestimation of both transmittance and wavelength at maximum.

Combined with previous sections, figure 5.9 not only measures the sensor's accuracy, but it also gives an idea of the physical properties for each cell. The lower the transmission, the greater its effective refractive index, due to a greater size, cytoplasmic index, nuclear radius or nuclear index. However, redshift has nothing to do with nuclear properties, and the greater its value, the bigger the cell or the higher its cytoplasmic index. Normally, cells located on the right side of the graph correspond to really big CTCs (high cytoplasmic index) with an important flattering, whereas the ones on the left tend to be small and barely deformed lymphocytes.

Chapter 6

Conclusions and Future Work

Over the last two decades, the phenomenon of extraordinary optical transmission has been proved to have powerful sensing applications. In this research, we take advantage of a periodically structured golden array with nanometric holes to excite such phenomenon and test the extent to which our device is sensitive to changes in the properties of the cells we locate on top of it. The behaviour of the sensor has been assessed by using two-dimensional computational models. From the preceding sections the following conclusions can be inferred:

1. The position of the EOT peak is only dependent upon the optical properties of the portion of cell inside the plasmon's penetration depth.

2. There exists a linear dependence of the wavelength at the EOT maximum with the cytoplasmic refractive index, flattering and area of cell within the penetration depth. Transmittance at maximum is linear with respect to the last two properties and quadratic with respect to the first one.

3. The plasma membrane has very little influence in the device's performance due to its negligible thickness and tiny variations from one cell to another. It does not affect the sensor's sensitivity and its consideration only increases insignificantly the effective refractive index of the cell.

4. The sensor is particularly sensitive to changes in the effective refractive index of the objects located on top of it (cell+buffer), resulting in a strong dependence on the cell size and index. The degree of contact plays an important role in the transmittance and wavelength of the EOT maximum, but nowhere near the effect of the effective refractive index. Furthermore, we report that it is the flattering and not the number of blocked holes what causes a change in the transmission spectrum.

5. A linear correlation between transmittance and wavelength at the EOT maximum has been reported for two samples of 50 lymphocytes and SW-480 CTCs, due to the negligible variances of the bibliographical cytoplasmic indices.

6. For a fixed wavelength, transmittance through the cell shows a decreasing tendency which is exponential for an increasing nuclear refractive index and polynomial under

positive variations of the nuclear size. It is therefore the nucleus what has a greater impact on the overall transmission of light through the cell due to its big size and high refractive index. On the contrary, there exist no effects of the nucleus on the wavelength at the EOT maximum due to its distance from the sensor, which is kept by the cytoskeleton. The position of the nucleus barely affects the transmittance and shows more variability for small nuclei.

7. Despite their huge nuclei, lymphocytes exhibit lower transmittance and wavelength changes than CTCs, due to their smaller size and effective refractive index. As a result, their position in the ΔT vs $\Delta\lambda$ map is restricted to a small portion located on the top left corner, close to the origin, whereas CTCs are significantly more dispersed.

8. A lower bound for the sensor's accuracy in order to discern lymphocytes and SW-480 CTCs was found to be 66%. In other words, assuming that the lymph is only composed by lymphocytes and CTCs, there exists a probability higher than 0.66 of telling whether the target cell from a lymph sample corresponds to that particular primary tumour.

The first step to improve the reliability of the results provided in this dissertation and, potentially, prove the assumed coupling between both geometrical models would be by developing a more powerful computational tool that enables a fine discretisation of the three-dimensional model for the film and the whole cell.

A straightforward continuation to this study would be to reproduce the same methods for different types of tumour cells. This would provide a map with a great deal of cell lines and depending on the region where each of them are located, diagnose the origin of the patient's anomalous cells and potentially use their genetic code to design treatments against them.

Experimentally, positive transmittance changes with respect to the free sensor have been found, that is to say, some cells exhibit greater transmission than the empty film. This apparent contradiction, due to the greater effective refractive index of the system cell+buffer, can be explained by the formation of air bubbles between the cell and the film, which are acting like optical lenses. As a consequence, more light could be focused on the spectrometer and a higher transmittance can be reported. Computationally, this could be simulated as a small air sphere underneath the cell.

However, this technique goes far beyond cancer diagnosis. As mentioned in chapter 3, the concentration of hemoglobin in blood can be easily determined using this device and a linear expression depending on the effective refractive index. Thus, this technique could also be used for anaemia diagnosis. Pregnancy tests could be significantly improved, as the current systems can only detect high enough concentrations of hormone hCG after six days of pregnancy. The large sensitivities of our sensor could allow to detect such hormone more prematurely. An interesting computational work to undertake would be the calculation of the actual concentration of hCG in blood to be detected by this device. We could therefore determine the precise time for a pregnant woman to be identified as such.

Bacteria present very different shapes and molecular compositions depending on their type. We could take advantage of this fact and create a ΔT vs $\Delta\lambda$ map for a few of them, which could be used as a diagnostic tool for bacterial diseases.

Previous research has been done on the sensing applications of Fabry-Perot nanocavities in which light reflects and interferes [4]. This could be studied through a similar configuration with an extra gold layer inside the glass substrate. The Fabry-Perot resonances occurring in the system along with EOT increase the sensitivity of the device. An interesting study to undertake would be the addition of this extra gold layer to measure the response when different cells are located on top.

Bibliography

[1] Abdelsalam, M.E, Bartlett, P.N., Kelf, T., Baumberg, J. "Wetting of Regularly Structured Gold Surfaces". Langmuir vol. 21(5) (2005). pp. 1753–1757.

[2] Albella, P., Moreno, F., Saiz, J.M., González, F. "Backscattering of metallic microstructures with small defects located on flat substrates". Optics Express vol. 15(11) (2007). pp. 6857–6867.

[3] Alberts, B. et al. "Molecular Biology of the Cell" 5th edition [Garland Science, 2008].

[4] Ameling, R. et al. "Cavity-enhanced Localized Plasmon Resonance Sensing". Applied Physics Letters vol.97 (2010).

[5] Bethe, H.A. "Theory of Diffraction by Small Holes". The Phys. Rev. vol. 66 (1944). pp. 163-182.

[6] Barreda, A.I. et al. "Electromagnetic Behavior of Dielectric Objects on Metallic Periodically Nanostructured Substrates". Optics Express vol. 26(9) (2018). pp. 11222-11237.

[7] Berthier, S., Lafait, J. "Effective Medium Theory: Mathematical Determination of the Physical Solution for the Dielectric Constant". Optics Communications Vol. 33(3) (1980). pp. 303-306.

[8] Bolsover, S.R. et al. "Cell Biology" 2nd edition [Jonh Wiley & Sons, 2004].

[9] Casas, J. "Óptica"[Pons, 1985].

[10] Coumans, F.A.W. et al. "Filter Characteristics Influencing Circulating Tumor Cell Enrichment from Whole Blood". PLoS ONE vol.8(4) (2013).

[11] Ebbesen, T.W., Lezec, H.J., Ghaemi, H.F., Thio, T., Wolff, P.A. "Extraordinary Optical Transmission through Sub-wavelength Hole Arrays". Nature vol. 391 (1998). pp. 667-669.

[12] Enoch, S., Bonod, N. "Plasmonics" [Springer 2012].

[13] Ghaemi, H.F., Ebbesen, T.W., Lezec, H.J. "Surface Plasmons Enhance Optical Transmission through Subwavelength Holes". Phys. Rev. B vol. 58 (1998). pp. 6779-6782.

[14] Gundersen, G.G., Worman, H.J. "Nuclear Positioning". Cell vol. 152 (2013). pp. 1376-1389.

[15] Homola, J. "Surface Plasmon Resonance Sensors for Detection of Chemical and Biological Species". Chem. Rev. Vol. 108 (2008). pp. 462-493.

[16] Johnson, P. B., Christy, R. W. "Optical Constants of the Noble Metals". Phys. Rev. B vol. 6 (1972). pp. 4370-4379.

[17] Kittel, C. "Introduction to Solid State Physics" [John Wiley & Sons, 2005].

[18] Krebs, M.G., et al. "Circulating Tumour Cells: their Utility in Cancer Management and Predicting Outcomes". Therapeutic Advances in Medical Oncology vol. 2(6) (2010). pp. 351-365

[19] Krupin, O., Berini, P. "Long-Range Surface Plasmon-Polariton Waveguide Biosensors for Human Cardiac Troponin I Detection". Sensors vol. 19 (2019). pp. 631-642.

[20] Liu, P.Y. et al. "Cell Refractive Index for Cell Biology and Disease Diagnosis: Past, Present and Future". The Royal Society of Chemistry vol. 16 (2016). pp. 634-644.

[21] Maier, S."Plasmonics: Fundamentals and Applications" [Springer, 2007].

[22] McMahon, J.M., Henzie, J., Odom, T.W., Schatz, G.C., Gray, S.K. "Tailoring the Sensing Capabilities of Nanohole Arrays in Gold Films with Rayleigh Anomaly-Surface Plasmon Polaritons". Optics Express vol. 15(26) (2007).

[23] Monteiro, J.,P. et al."Effect of Periodicity on the Performance of Surface Plasmon Resonance Sensors Based on Subwavelength Nanohole Arrays". Sensors and Actuators B vol. 178 (2013). pp. 366–370.

[24] Niklasson, G. A., Granqvist, C. G., Hunderi, O. "Effective Medium Models for the Optical Properties of Inhomogeneous Materials". Applied Optics vol. 20(1) (1981). pp. 26-30.

[25] Pravin, D.P., Navjeet, K.L. "Role of Circulating Tumor Cells in Future Diagnosis and Therapy of Cancer". Journal of Cancer Metastasis and Treatment vol. 1(2) (2015). pp. 44-56.

[26] Raether, H. "Surface Plasmons on Smooth and Rough Surfaces and on Gratings" [Springer-Verlag, 1988].

[27] Rodrigo, S. "Optical Properties of Nanostructured Metallic Systems" [Springer-Verlag, 2012].

[28] Wang, M., Pan, N. "Predictions of Effective Physical Properties of Complex Multiphase Materials". Materials Science and Engineering R vol. 63 (2008). pp. 1–30

[29] Wang, Y., Zhou, Y., Hu, Z. "The Functions of Circulating Tumor Cells in Early Diagnosis and Surveillance during Cancer Advancement". Journal of Translational Internal Medicie vol. 5(3) (2017). pp. 135-138.